

# Supersonic flow kinetics: Mesoscale structures, thermodynamic nonequilibrium effects and entropy production mechanisms

Yanbiao Gan<sup>1</sup>, Zhaowen Zhuang<sup>1</sup>, Bin Yang<sup>2</sup>, Aiguo Xu<sup>3,4,5,6</sup>, Dejia Zhang<sup>7†</sup>,  
Feng Chen<sup>8‡</sup>, Jiahui Song<sup>9</sup>, and Yanhong Wu<sup>1</sup>

<sup>1</sup>Hebei Key Laboratory of Trans-Media Aerial Underwater Vehicle, North China Institute of  
Aerospace Engineering, Langfang 065000, China

<sup>2</sup>School of Energy and Safety Engineering, Tianjin Chengjian University, Tianjin 300384,  
China

<sup>3</sup>National Key Laboratory of Computational Physics, Institute of Applied Physics and  
Computational Mathematics, P. O. Box 8009-26, Beijing 100088, China

<sup>4</sup>National Key Laboratory of Shock Wave and Detonation Physics, Mianyang 621999, China

<sup>5</sup>HEDPS, Center for Applied Physics and Technology, and College of Engineering, Peking  
University, Beijing 100871, China

<sup>6</sup>State Key Laboratory of Explosion Science and Technology, Beijing Institute of Technology,  
Beijing 100081, China

<sup>7</sup>School of Physical Science and Technology, Guangxi University, Nanning 530004, China

<sup>8</sup>School of Aeronautics, Shan Dong Jiaotong University, Jinan 250357, China

<sup>9</sup>School of Aerospace Engineering, Beijing Institute of Technology, Beijing 100081, China

(Received xx; revised xx; accepted xx)

Supersonic flow is a typical nonlinear, nonequilibrium, multiscale, and complex phenomenon. Compared to scenarios described by Navier-Stokes (NS) theory, mesoscale behavior in supersonic flow exhibits greater discreteness and a higher degree of nonequilibrium. Meanwhile, the entropy production mechanism, which involves compression efficiency and the ability to perform external work, is a significant focus in supersonic flow fields. As the degree of discrete/nonequilibrium effects increases, the study of entropy production based on NS theory may need reevaluation and appropriate revision. To address these issues, this paper develops and applies the discrete Boltzmann *modeling and analysis* method/model (DBM), based on kinetic and mean-field theories, to simulate, and analyze these phenomena. The study provides the following results: A Burnett-level DBM suitable for supersonic flow is constructed based on the Shakhov-BGK model. Higher-order analytical expressions for typical thermodynamic nonequilibrium

† Email address for correspondence: zdj202479@gxu.edu.cn

‡ Email address for correspondence: chenfeng-hk@sdjtu.edu.cn

effects are derived, providing a constitutive basis for improving traditional macroscopic hydrodynamics modeling. Criteria for evaluating the validity of DBM are established by comparing numerical and analytical solutions of nonequilibrium effects. The multi-scale DBM is used to investigate discrete/nonequilibrium characteristics and entropy production mechanisms in shock regular reflection. The findings include: (a) Compared to the NS-level DBM, the Burnett-level DBM offers more accurate representations of viscous stress and heat flux, i.e., more precise dissipative mechanisms, ensures non-negativity of entropy production in accordance with the second law of thermodynamics, and exhibits better numerical stability. (b) Near the interfaces of incident and reflected shock waves, strong nonequilibrium driving forces lead to prominent nonequilibrium effects. By monitoring the timing and location of peak nonequilibrium quantities, the evolution characteristics of incident and reflected shock waves can be accurately and dynamically tracked. (c) In the intermediate state, the bent reflected shock and incident shock interface are wider and exhibit lower nonequilibrium intensities compared to their final state. This observation can be used to track the position and straightening process of the bent shock. (d) The Mach number enhances various kinds of nonequilibrium intensities in a power-law manner  $D_{m,n} \sim \text{Ma}^\alpha$ . The power exponent  $\alpha$  and the order of nonequilibrium effects (kinetic modes)  $m$  follows a logarithmic relation  $\alpha \sim \ln(m - m_0)$ . This research provides new perspectives and kinetic insights into supersonic flow studies.

**Key words:** supersonic flow, discrete Boltzmann method, mesoscale structure, thermodynamic nonequilibrium effect, entropy production mechanism

---

## 1. Introduction

Supersonic flow, characterized by nonlinearity, nonequilibrium, and multiscale effects (Pham-Van-Diep *et al.* 1989), is widely observed in nature, scientific experiments, and defense engineering. It is significant not only in fundamental scientific research but also plays a crucial role in various key national strategic areas. For instance, in the energy sector, supersonic flow enhances both combustion efficiency and energy conversion efficiency (Law 2010). In aerospace engineering, supersonic technology is crucial for achieving high-speed flight and deep-space exploration (Wang *et al.* 2023, 2024; Wang & Wang 2024). In inertial confinement fusion, isotropic supersonic flow serves as a key mechanism for achieving high-efficiency fusion reactions (Zhou 2017*a,b*).

Supersonic flow exhibits diverse mesoscale structures (Huang & Edwards 2018) and kinetic modes that vary spatially and temporally. The interaction between these structures

and modes results in complex, significant, and persistent hydrodynamic nonequilibrium (HNE) and thermodynamic nonequilibrium (TNE) effects and behaviors (Xu & Zhang 2022; Xu *et al.* 2024). For instance, during re-entry into the upper atmosphere, a spacecraft transitions through the rarefied free-molecular flow regime, transitional flow regime, and slip flow regime, ultimately entering a relatively dense continuous flow regime at very high Mach numbers (Li & Zhang 2009; Li *et al.* 2015). significant cross-scale rarefied gas effects. The gas properties differ completely across each flow regime, with flow states exhibiting significant cross-scale rarefied gas effects. The continuous transition between different flow mechanisms requires the model to have cross-regime adaptability, both in terms of Knudsen number and the degree of nonequilibrium. Moreover, due to the interaction between supersonic flow and aircraft, various mesoscale structures and TNE behaviors exist around supersonic vehicles, such as bow shocks, shock/boundary layer interactions, shear layers (instabilities, transitions, impacts, reattachment), viscous disturbances, turbulent transitions, shock disturbances, flow separation, radiation, dissociation/ionization, and surface ablation. In near-space hypersonic vehicles, shock reflection and wave interference occur in the scramjet engine inlet duct and on both large components and small local objects of the aircraft, resulting in complex mesoscale structures such as incident shocks, reflected shocks, detached shocks, reattached shocks, and separation bubbles (Chang *et al.* 2017; Huang *et al.* 2020; Sawant *et al.* 2022; Bao *et al.* 2022).

These mesoscale structures and behaviors in supersonic flow exhibit both increased discreteness and a higher degree of nonequilibrium, which notably influence the system's evolutionary trajectory. prominent cross-scale rarefied gas effects This is because: (1) near strong discontinuities like shock waves, local characteristic scales decrease sharply, amplifying discrete effects and spatial multiscale phenomena; (2) the highly transient, strongly coupled, and unsteady nature of supersonic flows manifests that the system's flow characteristic time is no longer negligible compared to thermodynamic relaxation time, preventing timely relaxation to thermodynamic equilibrium. Additionally, these mesoscale structures and behaviors are closely correlated with entropy production (Zhang *et al.* 2016), a critical parameter for evaluating aerodynamic drag, compression efficiency, and the ability to perform external work in supersonic flow (Song *et al.* 2023). As the levels of nonequilibrium and discreteness increase, traditional entropy production studies based on Navier-Stokes (NS) theory may require reassessment and approximate revision. Recent studies (Rinderknecht *et al.* 2018; Cai *et al.* 2021; Shan *et al.* 2021) highlight that mesoscale kinetic phenomena, marked by significant nonequilibrium effects and discreteness, have a substantial impact on the success of ignition in ICF. Therefore, developing accurate, reliable, and efficient cross-scale models to quantitatively and dy-

namically characterize the evolution of mesoscale structures, nonequilibrium effects and entropy production mechanisms, clarify the formation mechanisms and evolution laws of these structures, and understand their impact on flow, heat transfer behaviors, is crucial for the cross-scale regulation of complex supersonic flow behaviors.

The primary approaches to studying nonequilibrium effects in supersonic flows include theoretical analysis, engineering experiments, and numerical simulations (Chen *et al.* 2019). Theoretical analysis involves solving and analyzing nonlinear equations that describe supersonic flow, such as the Euler, NS, Burnett, and super-Burnett equations. This approach often necessitates making numerous unreasonable simplifying assumptions, and most analytical solutions are confined to low-dimensional cases. Additionally, the strong nonequilibrium effects in supersonic flow lead to significant nonlinear coupling between multiple physical fields, further challenging the validity of these equations. The extreme complexity of flow configurations at supersonic flows also poses substantial challenges to theoretical analysis.

Engineering experiments, including flight and ground wind tunnel tests, are essential for studying nonequilibrium effects in supersonic flow (Jiang *et al.* 2020; Gu & Olivier 2020). While flight tests provide first-hand data and directly validate the feasibility of aircraft designs, they are both costly and technically challenging. Given the highly complex supersonic flow conditions in actual flight, ground wind tunnel tests are often replicate only certain aspects of these conditions. As a result, many ground tests cannot accurately simulate effects caused by high Reynolds number inflows, rarefied gas dynamics, and high-enthalpy conditions. This discrepancy often leads to a mismatch between flow states observed in ground tests and those in actual flight, significantly reducing the value of ground-based experiments.

Even with the successful execution of the aforementioned tests and experiments, significant challenges remain in measuring and analyzing nonequilibrium effects in supersonic flows. (1) *Extremes of spatiotemporal scales and limitations of measurement equipment:* Nonequilibrium effects typically manifest over very short timescales and within extremely small spatial regions. For example, rapid changes in temperature, density, and pressure across shock waves can occur within nanoseconds and be confined to micrometer-sized areas. These extreme temporal and spatial scales impose stringent requirements on the response time and resolution of experimental equipment. Traditional measurement instruments, such as pressure probes and thermocouples, often fail to accurately capture these changes within such short timescales and small regions, leading to imprecise or erroneous measurements. Optical measurement techniques (Danehy *et al.* 2015), while offering higher spatiotemporal resolution, often rely on the transparency and uniformity of the flow medium. In the complex environment of supersonic flows, measurement accu-

racy may be constrained. Furthermore, non-contact measurement methods, such as laser interferometry and particle image velocimetry, still encounter difficulties in capturing rapidly changing small-scale nonequilibrium phenomena due to high signal noise and complex data processing. (2) *Complexity of data interpretation and signal processing*: Even if experimental data are obtained, interpreting them remains a significant challenge. Nonequilibrium effects are often accompanied by strong signal fluctuations and complex background noise, making it difficult for traditional data processing methods to extract meaningful information. Furthermore, since nonequilibrium phenomena involve multi-scale and multiphysics coupling, data interpretation typically requires the integration of various theoretical models and numerical simulations, further increasing the complexity of data analysis. *Currently, the effective observation and quantitative analysis of these small-scale structures and fast modes remain key challenges in experimental fluid mechanics.* Consequently, the complexity of TNE effects and entropy production mechanisms within such flows remains poorly understood to date.

Compared to engineering tests, numerical simulations offer advantages such as lower cost, high repeatability, greater efficiency, reduced risk, adjustable parameters, comprehensive flow field information, and ease of analysis, making them essential tools for studying nonequilibrium effects in supersonic flows. Depending on the underlying physical models, numerical simulations can be classified into three scales: macroscopic, microscopic, and mesoscopic. Macroscopic-scale simulations rely on conservation equations derived from the continuity assumption and near-equilibrium approximations, including the Euler, NS, Burnett, and super-Burnett equations. The Euler equations, based on equilibrium assumptions, cannot describe TNE effects. The NS equations, based on near-equilibrium assumptions, incorporate linear constitutive relations (first-order viscous stress and heat flux terms) to represent TNE effects. However, in supersonic cross-regime flows, the effects of deviating from thermodynamic equilibrium are highly complex, profound, and multifaceted. Simply adding viscosity and heat conduction terms to the hydrodynamic equations, particularly linear ones, is insufficient to capture these effects accurately. As a result, the Euler and NS equations are applicable only to studying supersonic flows in continuous flow regimes ( $Kn < 0.001$ ) where nonequilibrium effects are relatively weak. For the slip-transition regime, the Burnett and super-Burnett equations, derived from second- and third-order Chapman-Enskog expansions of the velocity distribution function near thermodynamic equilibrium, theoretically cover continuous, slip, and parts of the transitional regimes with Knudsen numbers less than 1. However, these generalized macroscopic equations still encounter significant challenges in practical applications, including numerical instability at high Knudsen numbers, small wavelength instability with grid refinement, high nonlinearity, difficulty in satisfying entropy condi-

tions, complex boundary conditions, intricate programming, and low parallel computing efficiency. As a representative microscopic method, molecular dynamics (MD) simulation is particularly effective for studying nonequilibrium effects in supersonic flows at small scales (Liu *et al.* 2016, 2017). The strength of this method lies in its ability to account for the microscopic structure and dynamic behavior of molecules, thereby providing more accurate descriptions and predictions. However, due to high computational costs and limited spatial and temporal scales, MD is less suitable for large-scale, long-duration simulations, often requiring integration with other methods for a more comprehensive analysis.

As a mesoscopic approach bridging microscopic and macroscopic methods, the Boltzmann equation links interactions across scales by describing the spatiotemporal evolution of molecular velocity distributions, serving as a key component in kinetic theory framework and addressing TNE effects across the full spectrum of flow regimes. Kinetic modeling methods based on the Boltzmann equation for studying multiscale nonequilibrium flows can be broadly classified into the following four categories. (1) Kinetic macroscopic modeling: This method involves deriving macroscopic hydrodynamic equations (MHEs) through Chapman-Enskog multiscale analysis and Hermite polynomial expansion of the Boltzmann equation, followed by numerical solutions of these equations (Struchtrup 2005; Zhao *et al.* 2014). Consequently, the physical capabilities of these methods are confined to the scope described by the MHEs. It is important to note that MHEs can be divided into two categories: those involving only conserved moments, such as the Burnett and super-Burnett equations, and extended MHEs that include the evolution of both conserved and some non-conserved moments, such as Grad's 13-moment equations (Struchtrup & Torrilhon 2003), the Eu method (Eu 1992), and the nonlinear coupled constitutive relations method (Li & Xiao 2021; Rana *et al.* 2021; Jiang *et al.* 2019). (2) Kinetic direct modeling: This approach directly simulates the (modified or original) Boltzmann equation without deriving or solving MHEs, as in the direct simulation Monte Carlo (DSMC) method (Moss & Bird 2005; Schwartzentruber & Boyd 2015). The DSMC method models gas dynamics in nonequilibrium states by tracking the trajectories and collisions of gas molecules, making it particularly suitable for high Knudsen number flows. In situations where experimental data are difficult to obtain, DSMC simulation results are often considered a reliable approximation of experimental outcomes. However, due to constraints on grid cell size and time step (which must be smaller than the mean free path and particle collision time, respectively), the DSMC method becomes computationally intensive and memory-demanding when simulating near-continuum flows. (3) Direct solution of the Boltzmann equation: This category includes methods such as the discrete velocity method (Li & Zhang 2009; Yang *et al.* 2016), Fourier spectral method, and

fast spectral method (Wu *et al.* 2015). From a physical perspective, directly solving the original Boltzmann equation numerically preserves its physical properties to the greatest extent. These methods, however, face challenges, including high computational costs, significant memory requirements, dependence on specific boundary conditions, and complexity in algorithm implementation. (4) Kinetic discrete scheme method: Recent advances in kinetic discrete scheme methods have enhanced the study of nonequilibrium flows. Methods in this category include the gas kinetic scheme, unified gas kinetic scheme, discrete unified gas kinetic scheme, unified gas kinetic particle method, and unified gas kinetic wave particle method (Xu 2014; Xu & Huang 2010; Guo *et al.* 2015; Zhu *et al.* 2019), etc. While these methods have proven effective, they also pose challenges, including computational complexity, implementation difficulty, and, in some cases, substantial demands on computational resources.

Despite significant progress in kinetic modeling based on the Boltzmann equation, “*how to accurately describe*” and “*how to visually analyze*” mesoscopic states and effects remain major challenges in the numerical study of supersonic flows. Compared with the macroscopic state, the mesoscopic states exhibit a higher degree of discreteness and TNE. As a result, more variables are required to fully characterize the mesoscopic state. In terms of description, most kinetic methods currently still adhere to traditional macroscopic approaches, focusing primarily on a few physical quantities in the NS model, such as slow variables, conserved quantities, and a limited number of lower-order non-conserved quantities, lacking novel perspectives. As the degree of discretization and TNE increases, the complexity and uncertainty of system behaviors escalate, necessitating the inclusion of additional physical quantities and broader perspectives, particularly fast variables and higher-order non-conserved quantities across various scales. On the analytical side, it is urgent to develop methods for clearly and intuitively extracting and presenting information from complex nonequilibrium physical fields, as this will determine the depth and effectiveness of research. The technical key is how to achieve an intuitive geometric correspondence in the description of states and behaviors in complex systems. Commonly used measures of nonequilibrium in traditional fluid dynamics, such as the Knudsen number, viscosity, heat conduction, and macroscopic gradients, each describe the system’s nonequilibrium state from a specific perspective. However, these measures are highly condensed, averaged, and coarse-grained, often obscuring specific details about the nonequilibrium state that are crucial for in-depth analysis.

To tackle these challenges, we use the discrete Boltzmann method/modeling/model (DBM) developed by our research group (Xu *et al.* 2012; Xu & Zhang 2022; Xu *et al.* 2024). DBM is essentially a coarse-grained modeling and analysis method that combines kinetic theory with mean field theory. Historically, DBM evolved from the physical

modeling branch of the lattice Boltzmann method (LBM) (Succi 2018; Guo & Shu 2013; Wei *et al.* 2022), selectively retaining, discarding, and enhancing various aspects. Unlike traditional fluid modeling, DBM does not rely on the continuity assumption or near-equilibrium approximations. It no longer uses the standard “lattice gas” imagery of the LBM, nor does it combine with specific discretization schemes (Wang *et al.* 2020, 2022). Instead, it introduces kinetic schemes for detecting, presenting, describing, and analyzing nonequilibrium states and effects based on phase space theory. As the degree of discretization and nonequilibrium increases, DBM distinguishes itself from traditional modeling methods and other kinetic approaches by incorporating more kinetic modes in physical modeling and utilizing higher-order non-conserved quantities, particularly TNE quantities, in physical analysis to describe system states and behaviors. Consequently, from a modeling perspective, DBM is a direct kinetic modeling approach, while from the perspective of complex physical field analysis, it serves as a kinetic analysis method.

In recent years, DBM has made significant advances in the study of nonequilibrium flows and transport mechanisms, with applications in high-speed compressible flows (Gan *et al.* 2013, 2018; Bao *et al.* 2022; Qiu *et al.* 2020, 2021, 2024), multiphase flows (Gan *et al.* 2015, 2022; Zhang *et al.* 2019b), fluid instabilities (Gan *et al.* 2019; Lai *et al.* 2016; Chen *et al.* 2024a,b), micro- and nanoscale flows (Zhang *et al.* 2023), chemically reactive flows (Lin *et al.* 2017; Ji *et al.* 2022), and plasma kinetics (Liu *et al.* 2023; Song *et al.* 2024). The gradual advancement of DBM research from the “shallow water” regime (small Kn number) to the “deep water” regime (increasing Kn number) is an ongoing effort we have been making in recent years (Gan *et al.* 2018, 2022; Zhang *et al.* 2019a, 2022; Song *et al.* 2023, 2024; Shan *et al.* 2023). For example, DBM has successfully reproduced and kinetically clarified heat conduction behavior in square cavity flow (Zhang *et al.* 2019a) and following strong shock wave (Shan 2024), phenomena that appear to violate Fourier’s law. DBM studies reveal that nonequilibrium effects near mesoscale structures, such as material, shock wave, and liquid-vapor interfaces, exhibit strong nonlinearity. The relative strength of higher- and lower-order nonequilibrium effects is significant, with higher-order nonequilibrium influencing lower-order effects through a complex feedback relationship (Gan *et al.* 2018, 2022). In the steady-state DBM, which focuses on steady-state behavior, the distribution function transitions from accounting for only partial Kn number effects in the time-dependent scenarios to including all Kn number effects (Zhang *et al.* 2023). It should be noted that the mesoscale temporal behavior, sandwiched between macroscopic continuous modeling and molecular dynamics, remains poorly understood.

In supersonic flows, as Mach numbers increase, compressibility intensifies, rarefied gas effects become more pronounced, complex interfaces arise, and small-scale structures emerge, the types, magnitudes, and durations of nonequilibrium driving forces in the



system multiply. This necessitates reassessing the validity of existing DBM models and reconsidering current research perspectives and analytical approaches. Therefore, this paper seeks to further explore the following questions: (1) How to accurately, efficiently, and conveniently identify and incorporate the necessary kinetic modes under these extreme conditions to precisely describe strong nonequilibrium effects? (2) How to derive theoretical expressions for higher-order nonequilibrium effects influenced by multiple physical fields? (3) How to develop cross-scale DBM suitable for complex fluid systems with higher discretization and stronger nonequilibrium effects? (4) How to design coupling and switching criteria for multiscale DBM to achieve adaptive and efficient simulations of multiscale problems? (5) How to adjust perspectives on nonequilibrium effect descriptions, enhance analysis methods for nonequilibrium behaviors, and expand the depth and breadth of research into nonequilibrium effects? (6) Finally, how to use DBM simulations and phase-space analysis method to clarify the nonequilibrium characteristics and evolution mechanisms of mesoscale structures in supersonic flows, as well as their impact on flow, heat transfer, and entropy production mechanisms?

## 2. Physical modeling of thermodynamic nonequilibrium effects

The DBM encompasses two critical components: modeling TNE effects and extracting, presenting, and analyzing these effects. The accuracy in describing TNE effects directly determines the model's precision, as TNE effects are fundamental characteristics of multiscale systems, which are intrinsically tied to the constitutive relations of the fluid system and their evolution.

TNE effects consist of two primary aspects: spatial nonequilibrium (discrete effects) and temporal nonequilibrium (related to relaxation time). TNE effects exhibit a dual nature. On one hand, they represent a hallmark of nonequilibrium characteristics, reflecting the complexity of the system. On the other hand, they act as the driving force for system evolution. TNE effects and mesoscale structures are deeply coupled and mutually influential. Their interactions can be classified into: (1) driving and formation, (2) enhancement and feedback, (3) stabilization and self-organization, (4) competition and selection, (5) feedback and regulation. In this section, we discuss how to realize multiscale modeling and analyzing TNE effects via DBM.

### 2.1. *Thermodynamic nonequilibrium effects: view from macroscopic hydrodynamic equations and DBM*

By performing the Chapman-Enskog multi-scale analysis on the Boltzmann-BGK equation, macroscopic hydrodynamic equations (MHEs) can be derived. To simplify the complex collision term in the original Boltzmann equation and adjust the Prandtl

number, a linearized collision term with Shakhov model is used (Shakhov 1968)

$$\frac{\partial f}{\partial t} + \mathbf{v} \cdot \nabla f = -\frac{1}{\tau}(f - f^S), \quad (2.1)$$

where  $f$ ,  $\mathbf{v}$ , and  $\tau$  denote the distribution function, particle velocity, and relaxation time, respectively. In fact, the BGK operator employed in nonequilibrium flow research is modified using mean-field theory (Gan *et al.* 2022; Xu *et al.* 2024). The Shakhov distribution function is given by  $f^S = f^{eq} + f^{eq}\{(1 - \text{Pr})\mathbf{v}^* \cdot \mathbf{q}[\frac{\mathbf{v}^{*2} + \eta^2}{RT} - (D + n + 2)] / [(D + n + 2)PRT]\}$ , where  $\text{Pr}$ ,  $\mathbf{q}$ ,  $R$ ,  $T$ ,  $P (= \rho RT)$ , and  $D$  represent the Prandtl number, heat flux, gas constant, temperature, pressure, and spatial dimension, respectively.  $\mathbf{v}^* = \mathbf{v} - \mathbf{u}$  is the thermo-fluctuation velocity and  $\mathbf{u}$  the fluid velocity.  $\eta^2 = \sum_{j=1}^n \eta_j^2$ , with  $\eta_j$  being a free parameter introduced to account for the  $n$  extra degrees of freedom corresponding to molecular rotation and/or vibration. Finally,  $f^{eq} = \rho(\frac{1}{2\pi RT})^{(D+n)/2} \exp[-\frac{\mathbf{v}^{*2}}{2RT} - \frac{\eta^2}{2RT}]$  represents the Maxwell equilibrium distribution function. The Shakhov model adds a nonequilibrium term into the distribution function to adjust energy transport, thereby partially addressing the BGK model's limitation of a fixed Prandtl number ( $\text{Pr} = 1$ ). This enhancement allows for a more accurate depiction of system behavior under nonequilibrium conditions. While utilizing  $f^S$  instead of  $f^{eq}$  increases the complexity of the collision term, this added complexity is essential for achieving greater physical accuracy. Consequently, practical applications should carefully balance computational complexity and the desired level of accuracy in the results.

Applying Chapman-Enskog expansion to both sides of equation (2.1) yields the following extended MHEs:

$$\begin{cases} \partial_t \rho + \nabla \cdot (\rho \mathbf{u}) = 0, \\ \partial_t (\rho \mathbf{u}) + \nabla \cdot (\rho \mathbf{u} \mathbf{u} + P \mathbf{I} + \mathbf{\Delta}_2^*) = 0, \\ \partial_t (\rho e) + \nabla \cdot [(\rho e + P) \mathbf{u} + \mathbf{\Delta}_2^* \cdot \mathbf{u} + \mathbf{\Delta}_{3,1}^*] = 0. \end{cases} \quad (2.2)$$

Here,  $e = c_v T + u^2/2$  the specific total energy with  $c_v = (n + 2)R/2$  the specific heat at constant volume,  $\mathbf{\Delta}_2^*$  and  $\mathbf{\Delta}_{3,1}^*$  correspond to the generalized viscous stress and heat flux, respectively. These extended MHEs incorporate higher-order constitutive corrections, offering a more comprehensive representation of TNE phenomena and their impact on fluid dynamics.

Equation (2.2) demonstrates that MHEs describe TNE effects exclusively and implicitly through constitutive relations. In contrast, DBM captures TNE effects directly and explicitly via higher-order non-conserved moments of  $(f - f^{(0)})$ :

$$\mathbf{\Delta}_{m,n}^* = \mathbf{M}_{m,n}^*(f - f^{(0)}) = \int_{-\infty}^{\infty} \int_{-\infty}^{\infty} \left(\frac{1}{2}\right)^{1-\delta_{m,n}} (f - f^{(0)}) \underbrace{\mathbf{v}^* \mathbf{v}^* \cdots \mathbf{v}^*}_n (\mathbf{v}^{*2} + \eta^2)^{\frac{m-n}{2}} d\mathbf{v} d\eta_i, \quad (2.3)$$

where  $\mathbf{\Delta}_{m,n}^*$  represents  $m$ -th order tensors contracted to  $n$ -th order tensors, with

$\delta_{m,n}$  as the Kronecker delta function, and  $f^{(0)} = f^{eq}$ . When  $m = n$ ,  $\Delta_{m,n}^*$  reduces to  $\Delta_m^*$ . Replacing  $\mathbf{v}^*$  in equation (2.1) with  $\mathbf{v}$  converts the central moment  $\Delta_{m,n}^*$  into the non-central moment  $\Delta_{m,n}$ , which describe the combined effects of HNE and TNE, typically referred to as thermo-hydrodynamic non-equilibrium (THNE) effects. Additionally,  $\Delta_{m,n} - \Delta_{m,n}^*$  represents HNE effects, offering a valuable supplement to the description of nonequilibrium effects based on macroscopic gradients in traditional fluid mechanics. TNE measures ( $\Delta_2^*$  and  $\Delta_{3,1}^*$ ) in MHEs are typical ones as defined by equation (2.1), also known as non-organized moment flux (NOMF) and non-organized energy flux (NOEF).

Moreover, it can be observed that MHEs describe only the evolution of the three conserved moments  $(\rho, \rho\mathbf{u}, \rho e) = (\mathbf{M}_0(f), \mathbf{M}_1(f), \mathbf{M}_{2,0}(f))$ . Higher-order non-conserved moments of  $f$  are not included in traditional fluid dynamics. This has two implications: it simplifies macroscopic hydrodynamic descriptions but also creates challenges in accurately describing discontinuous or nonequilibrium flows. In contrast, recovering the corresponding level of MHEs is just one of the DBM's physical functions. Corresponding to the physical functions of DBM are the extended hydrodynamic equations (EHEs), which, in addition to equation (2.2), also include evolution equations for some of the most closely related non-conserved moments, such as,  $\mathbf{M}_2(f), \mathbf{M}_{3,1}(f), \mathbf{M}_3(f)$  and  $\mathbf{M}_{4,2}(f)$ , etc. The necessity of these extended parts (i.e., the evolution equations of the relevant non-conserved moments) increases rapidly with the degree of discretization and nonequilibrium, as they describe the evolution of nonlinear constitutive relations (equations (2.4) and (2.5)) and so on:

$$\partial_t \Delta_2^* + \partial_t \mathbf{M}_2^*(f^{(0)}) + \nabla \cdot \mathbf{M}_3^*(f^{(0)}) + \mathbf{M}_2^*(f^{(0)})\mathbf{u} + \Delta_3^* + \Delta_2^*\mathbf{u} + \frac{1}{\tau} \Delta_2^* = 0, \quad (2.4)$$

$$\partial_t \Delta_{3,1}^* + \partial_t \mathbf{M}_{3,1}^*(f^{(0)}) + \nabla \cdot \mathbf{M}_{4,2}^*(f^{(0)}) + \mathbf{M}_{3,1}^*(f^{(0)})\mathbf{u} + \Delta_{4,2}^* + \Delta_{3,1}^*\mathbf{u} + \frac{1}{\tau} \Delta_{3,1}^* = 0. \quad (2.5)$$

## 2.2. Derivation of thermodynamic nonequilibrium effects

The TNE measures,  $\Delta_{m,n}^*$ , are primarily unknown. To derive their explicit expressions, we perform the Chapman-Enskog expansion on both sides of equation (2.1) by introducing the following expansions:

$$\begin{cases} f = f^{(0)} + f^{(1)} + f^{(2)} + \dots, \\ f^S = f^{S(0)} + f^{S(1)} + f^{S(2)} + \dots, \\ \frac{\partial}{\partial t} = \frac{\partial}{\partial t_1} + \frac{\partial}{\partial t_2} + \dots, \\ \nabla = \nabla_1, \end{cases} \quad (2.6)$$

where  $f^{(j)}$ ,  $f^{S(j)}$ ,  $\partial_{t_j}$ ,  $\nabla_j$  represent the  $j$ -th order terms in the Knudsen number. By comparing the coefficients at each order, we obtain the first- and second-order deviations

of the distribution function:

$$f^{(1)} = -\tau \left( \frac{\partial f^{(0)}}{\partial t_1} + \mathbf{v} \cdot \nabla_1 f^{(0)} \right) + f^{S(1)}, \quad (2.7)$$

$$f^{(2)} = -\tau \left( \frac{\partial f^{(0)}}{\partial t_2} + \frac{\partial f^{(1)}}{\partial t_1} + \mathbf{v} \cdot \nabla_1 f^{(1)} \right) + f^{S(2)}. \quad (2.8)$$

Next, we derive the TNE expressions by using transformation relations for temporal and spatial derivatives at different scales,  $\partial t_j(\cdot)$  and  $\nabla_j(\cdot)$ , along with the kinetic moments of  $f^{S(j)}$ , given by  $\mathbf{M}_2(f^{S(n)}) = 0$  and  $\mathbf{M}_{3,1}(f^{S(n)}) = (1 - \text{Pr})\mathbf{q}^{(n)}$ .

After some straightforward but tedious algebraic manipulations, we obtain the following relations between thermodynamic forces and fluxes:

$$\Delta_2^{*(1)} = -\mu[\nabla \mathbf{u} + (\nabla \mathbf{u})^T - \frac{2}{n+2} \mathbf{I} \nabla \cdot \mathbf{u}], \quad (2.9)$$

$$\Delta_{3,1}^{*(1)} = -\kappa \nabla T, \quad (2.10)$$

where  $\mu = P\tau$  is the viscosity coefficient, and  $\kappa = c_p\mu/\text{Pr}$  is the thermal conductivity, with  $c_p = (n+4)R/2$  the specific heat at constant pressure. The expressions for the second-order constitutive relations,  $\Delta_2^{*(2)}$  and  $\Delta_{3,1}^{*(2)}$ , can be found in Appendix A. Consequently, the constitutive relations at the Burnett level are given by  $\Delta_2^* = \Delta_2^{*(1)} + \Delta_2^{*(2)}$  and  $\Delta_{3,1}^* = \Delta_{3,1}^{*(1)} + \Delta_{3,1}^{*(2)}$ , which are expected to significantly enhance macroscopic modeling. Similar derivations can be used to obtain counterparts and other TNE measures at and beyond the super-Burnett level.

Analysis of the above analytical expressions reveals that:

(i) TNE intensity depends on macroscopic quantities, their gradients, relaxation time, additional degrees of freedom, and the Prandtl number. Here, relaxation time characterizes temporal nonequilibrium, whereas gradients of macroscopic quantities describe spatial nonequilibrium or discreteness. As TNE intensity increases, the expressions incorporate more physical quantities and their gradients. This reflects a broader range of nonequilibrium driving forces and highlights the increasing complexity of these effects. For a detailed analysis, please refer to Appendix A.

(ii) As TNE intensity increases, the linear constitutive relations fail, a Newtonian fluid will transition into a non-Newtonian fluid. When higher-order TNE effects become non-negligible, the system exhibits characteristics akin to non-Newtonian fluids, such as shear thinning, shear thickening, thixotropy, viscoelasticity, and antithixotropy. These behaviors arise from different types of feedback from higher-order TNE effects on constitutive relations.

(iii) The Shakhov-BGK model adjusts the system's Prandtl number by introducing a heat flux term. However, this approach is only suitable for cases with weak TNE effects. As TNE intensity increases, the system's Prandtl number is no longer a fixed value

depending solely on material properties. Instead, it becomes a variable that also depends on the local state of the flow field. At this stage, a generalized expression can be defined as:  $\text{Pr}^* = \frac{\mu^* C_p^*}{\kappa^*}$ , where  $\mu^*$ ,  $C_p^*$ , and  $\kappa^*$  represent the effective dynamic viscosity, specific heat capacity, and thermal conductivity, respectively. These quantities can be expressed as corrections to their classical values:  $\mu^* = \mu + \Delta\mu(\partial_\alpha u_\beta, \partial_\alpha \rho, \partial_\alpha T, \dots)$ ,  $C_p^* = C_p + \Delta C_p(\partial_\alpha u_\beta, \partial_\alpha \rho, \partial_\alpha T, \dots)$ , and  $\kappa^* = \kappa + \Delta\kappa(\partial_\alpha u_\beta, \partial_\alpha \rho, \partial_\alpha T, \dots)$ , with  $\Delta\mu$ ,  $\Delta C_p$ , and  $\Delta\kappa$  the corrections to the dynamic viscosity, specific heat capacity, and thermal conductivity due to higher-order TNE effects, respectively. Additionally, specific expressions may also need to consider fluid properties, boundary conditions, and external field influences.

### 2.3. Determination of the most essential moments

The distribution functions  $f^{eq}$  and  $f^S$  possess an infinite number of kinetic moments, each describing different aspects of the fluid system's kinetic properties. In coarse-grained physical modeling, selecting kinetic moments corresponds to choosing the physical properties that the model aims to describe, which is a fundamental task in this approach (Gan *et al.* 2022). To derive MHEs at the Burnett level from the Boltzmann-BGK equation, nine independent kinetic moments of  $f^{eq}$  are used:  $\mathbf{M}_0$ ,  $\mathbf{M}_1$ ,  $\mathbf{M}_{2,0}$ ,  $\mathbf{M}_2$ ,  $\mathbf{M}_{3,1}$ ,  $\mathbf{M}_3$ ,  $\mathbf{M}_{4,2}$ ,  $\mathbf{M}_4$ , and  $\mathbf{M}_{5,3}$ . Additionally, the following seven independent kinetic moments of  $f^S$  are used:  $\mathbf{M}_0^S$ ,  $\mathbf{M}_1^S$ ,  $\mathbf{M}_{2,0}^S$ ,  $\mathbf{M}_2^S$ ,  $\mathbf{M}_{3,1}^S$ ,  $\mathbf{M}_3^S$ , and  $\mathbf{M}_{4,2}^S$ . Among these moments, the first three are conserved moments, while the others are non-conserved. The moments  $\mathbf{M}_3$ ,  $\mathbf{M}_{4,2}$ ,  $\mathbf{M}_2^S$ , and  $\mathbf{M}_{3,1}^S$  describe first-order TNE effects, while  $\mathbf{M}_4$ ,  $\mathbf{M}_{5,3}$ ,  $\mathbf{M}_3^S$ , and  $\mathbf{M}_{4,2}^S$  correspond to second-order TNE effects.

### 2.4. Discretizations of velocity space and equilibrium distribution function

The most essential moments are the invariants to be preserved in DBM coarse-grained physical modeling, i.e., these kinetic moments should remain consistent when transforming from integral form to summation form

$$\Phi_{m,n} = \int_{-\infty}^{\infty} \int_{-\infty}^{\infty} f^{(0)} \Psi(\mathbf{v}, \eta) d\mathbf{v} d\eta = \sum_i f_i^{(0)} \Psi(\mathbf{v}_i, \eta_i), \quad (2.11)$$

$$\Phi_{m,n}^S = \int_{-\infty}^{\infty} \int_{-\infty}^{\infty} f^S \Psi'(\mathbf{v}, \eta) d\mathbf{v} d\eta = \sum_i f_i^S \Psi'(\mathbf{v}_i, \eta_i), \quad (2.12)$$

where  $\Phi_{m,n} = [\mathbf{M}_0, \mathbf{M}_1, \mathbf{M}_{2,0}, \mathbf{M}_2, \mathbf{M}_{3,1}, \mathbf{M}_3, \mathbf{M}_{4,2}, \mathbf{M}_4, \mathbf{M}_{5,3}]$  and  $\Phi_{m,n}^S = [\mathbf{M}_0^S, \mathbf{M}_1^S, \mathbf{M}_{2,0}^S, \mathbf{M}_2^S, \mathbf{M}_{3,1}^S, \mathbf{M}_3^S, \mathbf{M}_{4,2}^S]$ . Correspondingly,  $\Psi(\mathbf{v}, \eta) = [1, \mathbf{v}, \frac{1}{2}(v^2 + \eta^2), \dots, \frac{1}{2}(v^2 + \eta^2)\mathbf{v}\mathbf{v}]$ , and  $\Psi'(\mathbf{v}, \eta) = [1, \mathbf{v}, \frac{1}{2}(v^2 + \eta^2), \dots, \frac{1}{2}(v^2 + \eta^2)\mathbf{v}\mathbf{v}]$ . By incorporating the additionally required kinetic moments into  $\Phi_{m,n}$  and  $\Phi_{m,n}^S$ , one can construct a DBM with the desired order of accuracy and perform simulations without needing the exact form of the extended MHEs. Compared to deriving and solving higher-order extended MHEs, the

complexity of constructing and computing DBM only increases slightly. For example, to achieve third-order accuracy in viscous stress and heat flux, incorporating  $\mathbf{M}_5$  and  $\mathbf{M}_{64}$  into  $\Phi_{m,n}$ , and  $\mathbf{M}_4^S$  and  $\mathbf{M}_{5,3}^S$  into  $\Phi_{m,n}^S$ , is sufficient. This makes DBM particularly suitable for multiscale fluid simulations.

Equations (2.11) and (2.12) can be reexpressed in matrix form as follows:

$$\Phi_{m,n} = \Psi \mathbf{f}^{(0)}, \quad (2.13)$$

$$\Phi_{m,n}^S = \Psi' \mathbf{f}^S. \quad (2.14)$$

Consequently, the discrete equilibrium distribution function (DEDF) vectors  $\mathbf{f}^{(0)}$  and  $\mathbf{f}^S$  can be computed as follows (Gan *et al.* 2013),

$$\mathbf{f}^{(0)} = \Psi^{-1} \Phi_{m,n}, \quad (2.15)$$

$$\mathbf{f}^S = \Psi'^{-1} \Phi_{m,n}^S, \quad (2.16)$$

where  $\Psi^{-1}$  and  $\Psi'^{-1}$  represent the inverses of  $\Psi$  and  $\Psi'$ , respectively. To improve the physical accuracy and computational stability of the model, we require that  $\mathbf{f}^{(0)}$  further satisfy the moment relation  $\mathbf{M}_{40}$ , and  $\mathbf{f}^S$  satisfy the moment relations  $\mathbf{M}_4^S$ ,  $\mathbf{M}_{5,3}^S$ , and  $\mathbf{M}_{40}^S$ . Thus,  $\Phi_{m,n} = (M_0, M_{1x}, M_{1y}, M_{2,0}, \dots, M_{5,3yyy}, M_{40})^T$ ,  $\Phi_{m,n}^S = (M_0^S, M_{1x}^S, M_{1y}^S, M_{2,0}^S, \dots, M_{5,3yyy}^S, M_{40}^S)^T$ ,  $\mathbf{f}^{(0)} = (f_1^{(0)}, f_2^{(0)}, \dots, f_{26}^{(0)})^T$ ,  $\mathbf{f}^S = (f_1^S, f_2^S, \dots, f_{26}^S)^T$ , where each vector has 26 components in the two-dimensional case. The matrix  $\Psi = \Psi' = (\mathbf{C}_1, \mathbf{C}_2, \dots, \mathbf{C}_{26})$  is a  $26 \times 26$  matrix linking the DEDF and the kinetic moments, with  $\mathbf{C}_i = [1, v_{ix}, v_{iy}, \dots, \frac{1}{2}(v_{ix}^2 + v_{iy}^2 + \eta_i^2)v_{iy}^3, \frac{1}{2}(v_{ix}^2 + v_{iy}^2 + \eta_i^2)^2]^T$ .

DBM uses a finite number of particle velocities to replace the continuous velocity space. After discretizing, the discrete form of equation (2.1) is:

$$\frac{\partial f_i}{\partial t} + \mathbf{v}_i \cdot \nabla f_i = -\frac{1}{\tau}(f_i - f_i^S). \quad (2.17)$$

The evolution equation (2.17) for  $f_i$  and the constraint equations (2.16)-(2.14) for the discrete velocities  $(\mathbf{v}_i, \boldsymbol{\eta}_i)$  together form the model equation of the DBM. In principle, the choice of discrete velocities is arbitrary, as long as the matrices  $\Psi$  and  $\Psi'$  are of full rank. In practical simulations, the discrete velocity stencil typically aims to improve numerical stability by maintaining high geometric symmetry while ensuring physical symmetry (i.e., satisfying the corresponding moment relations). Since the number of discrete velocities equals the number of independent moment relations, this discretization method is physically the most computationally efficient. Strictly speaking, discretizing the continuous space inevitably breaks physical symmetry, leading to inaccurate descriptions of system properties. Therefore, coarse-grained physical modeling inherently involves trade-offs: the system characteristics under study must be strictly preserved during discretization, while characteristics beyond the scope of the study can be selectively

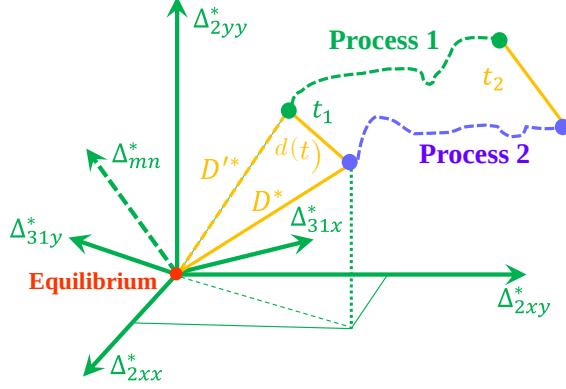


Figure 1: Schematic diagram of the phase space spanned by the independent components of the nonequilibrium characteristic quantity  $\Delta_{m,n}$ .

retained or sacrificed. Among the many options that meet the research needs, the simplest or most economical is often the preferred choice.

### 2.5. Extraction and exhibition of thermodynamic nonequilibrium effects

DBM is not only a multiscale modeling method for nonequilibrium flows but also an analysis tool for complex physical fields. In other words, it handles both pre-simulation physical modeling and post-simulation data analysis. To intuitively display complex field information, DBM has developed a scheme based on phase space for detecting, presenting, describing, and analyzing nonequilibrium states and effects. Specifically, DBM employs the independent components of non-conservative moments of  $(f - f^{eq})$ ,  $\Delta_{m,n}^*$ , to construct a high-dimensional phase space that describes the system's nonequilibrium states and effects, as illustrated in figure 1. In this phase space, the origin represents the equilibrium state, and any other point indicates a nonequilibrium state. The intercepts of this nonequilibrium state on each axis describe the degree and manner of the system's deviation from equilibrium from their respective perspectives. The distance from a nonequilibrium point to the origin roughly measures the degree of nonequilibrium, or the total nonequilibrium intensity,

$$D_T^* = \sqrt{\sum_{m,n} \Delta_{m,n}^{*2}}. \quad (2.18)$$

Accordingly, the dimensionless total nonequilibrium intensity is defined by

$$\tilde{D}_T^* = \sqrt{\sum_{m,n} (\Delta_{m,n}^*/T^{\frac{m}{2}})^2}. \quad (2.19)$$

The reciprocal of the distance between two points defines the similarity between two nonequilibrium states. Further, introducing a nonequilibrium intensity vector,  $\mathbf{S}_{TNE}$ ,

enables a multi-perspective description of the nonequilibrium state

$$\mathbf{S}_{\text{TNE}} = \left\{ \begin{array}{l} \Delta_{2xx}^*, \Delta_{2xy}^*, \Delta_{2yy}^*, \Delta_{3,1x}^*, \Delta_{3,1y}^*, \dots, \Delta_{5,3xyy}^*, \Delta_{5,3yyy}^*, \\ |\mathbf{\Delta}_2|, |\mathbf{\Delta}_{3,1}|, |\mathbf{\Delta}_3|, |\mathbf{\Delta}_{4,2}|, |\mathbf{\Delta}_4|, |\mathbf{\Delta}_{5,3}|, D_T^*, \tilde{D}_T^* \end{array} \right\}, \quad (2.20)$$

where the first line specifies the components of  $\mathbf{\Delta}_{m,n}$ , the second line quantifies the intensity of each TNE measure and the overall nonequilibrium strength. The phase space method, based on the non-conservative moments of  $(f - f^{eq})$ , provides clear, intuitive geometric representations of complex nonequilibrium states and behaviors, simplifying the understanding of complex systems and enabling detailed, quantifiable research of previously elusive information.

### 3. Numerical results and analysis

In this section, we first develop the first-order and second-order DBMs. Then, we validate the second-order model's ability to describe large-scale structures through a series of benchmarks, ranging from subsonic to hypersonic regimes. Next, we assess the model's effectiveness in capturing nonequilibrium effects across various orders. Finally, we investigate both HNE and TNE characteristics, along with entropy production mechanisms, during the regular reflection of shock waves.

To perform numerical simulations, it is necessary to design a set of discrete velocities to discretize the velocity space and ensure the existence of  $\Psi^{-1}$  and  $\Psi'^{-1}$ . Figure 2 illustrates the discrete velocity stencil, with the first-order DBM using the first 16 discrete velocities and the second-order DBM utilizing all 26 velocities:

$$(v_{ix}, v_{iy}) = \begin{cases} \text{cyc} : c(\pm 1, 0) & \text{for } 1 \leq i \leq 4 \\ c(\pm 1, \pm 1) & \text{for } 5 \leq i \leq 8 \\ \text{cyc} : 2c(\pm 1, 0) & \text{for } 9 \leq i \leq 12 \\ 2c(\pm 1, \pm 1) & \text{for } 13 \leq i \leq 16 \\ \text{cyc} : 3c(\pm 1, 0) & \text{for } 17 \leq i \leq 20 \\ 3c(\pm 1, \pm 1) & \text{for } 21 \leq i \leq 24 \\ c(a, b), -c(a, b) & \text{for } 25 \leq i \leq 26 \end{cases}, \quad (3.1)$$

where ‘‘cyc’’ indicates a cyclic permutation,  $c$  is an adjustable parameter controlling the size of discrete velocity, and  $a, b$  are free parameters. As a special case,  $a = 3$  and  $b = 1$  in figure 2. For the first-order DBM, when  $1 \leq i \leq 4$ ,  $\eta_i = \eta_0$ , and for all other  $i$ ,  $\eta_i = 0$ . For the second-order DBM, when  $1 \leq i \leq 4$ ,  $\eta_i = i\eta_0$ , and when  $13 \leq i \leq 20$ ,  $\eta_i = \eta_0$ ; otherwise,  $\eta_i = 0$ .

It is important to note that the physical model presented in Section 2, derived from coarse-grained modeling, does not include any specific discretization scheme. The choice of discrete velocities is a key technical aspect of DBM simulations. The discrete velocity



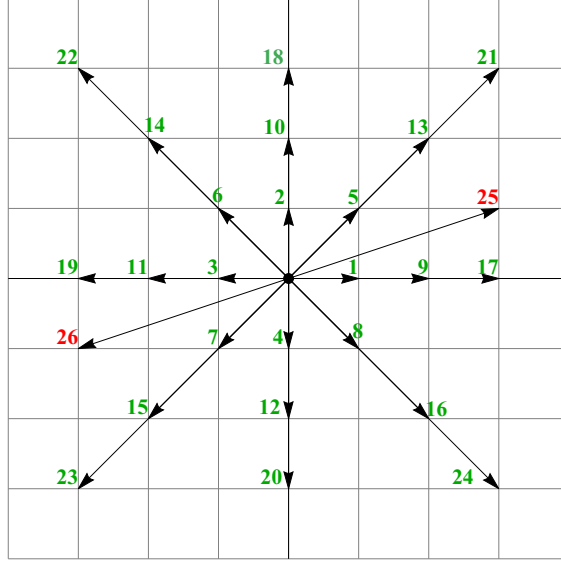


Figure 2: Sketch of the discrete velocity stencil. The first-order DBM uses the discrete velocities 1 – 16, and the second-order DBM uses the discrete velocities 1 – 26.

set in equation 3.1 is not a universal or optimal standard for all cases, but rather a method that meets the current research requirements. The selection of optimal discrete velocities is a complex problem involving the coupling of phase space discretization with temporal and spatial discretizations. In recent work, we aim to explore this issue in-depth via von Neumann stability analysis.

To improve numerical stability, efficiency, and accuracy in capturing complex multiscale structures, the third-order implicit-explicit Runge-Kutta finite difference scheme [94] is employed for time discretization; and depending on stability requirements, either the second-order non-oscillatory, parameter-free dissipative finite difference (FD) scheme or the fifth-order weighted essentially non-oscillatory FD scheme is applied for spatial discretization.

All physical quantities in the simulations are normalized using reference density  $\rho_0$ , reference temperature  $T_0$ , and reference length  $L_0$ :

$$\left\{ \begin{array}{l} \hat{\rho} = \frac{\rho}{\rho_0}, \quad \hat{r}_\alpha = \frac{r_\alpha}{L_0}, \quad \hat{T} = \frac{T}{T_0}, \quad (\hat{t}, \hat{\tau}) = \frac{(t, \tau)}{L_0/\sqrt{RT_0}}, \\ \hat{P} = \frac{P}{\rho_0 RT_0}, \quad (\hat{v}_\alpha, \hat{u}_\alpha) = \frac{(v_\alpha, u_\alpha)}{\sqrt{RT_0}}, \\ (\hat{f}, \hat{f}^S, \hat{f}^{eq}) = \frac{(f, f^S, f^{eq})}{\rho_0 (RT_0)^{-D/2}}, \\ (\hat{f}_i, \hat{f}_i^S, \hat{f}_i^{eq}) = \frac{(f_i, f_i^S, f_i^{eq})}{\rho_0}, \\ \hat{\kappa} = \frac{\kappa}{\rho_0 R L_0 \sqrt{RT_0}}, \quad \hat{\mu} = \frac{\mu}{\rho_0 L_0 \sqrt{RT_0}}. \end{array} \right. \quad (3.2)$$

Variables with “ $\hat{\ }$ ” on the left are dimensionless, while those on the right are dimensional. For simplicity, the dimensionless symbol “ $\hat{\ }$ ” is omitted in the rest of the paper.

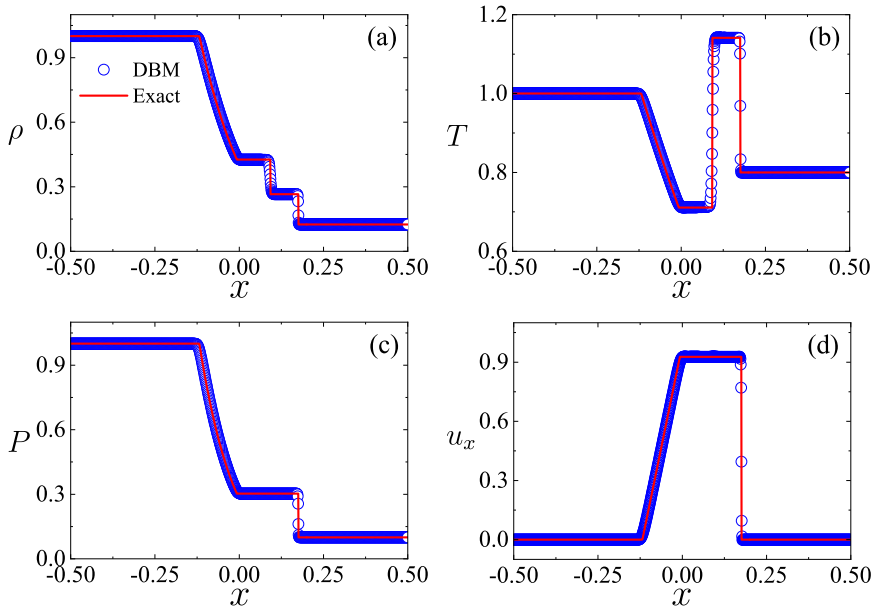


Figure 3: Comparison of DBM simulation results with Riemann solutions for the Sod shock tube problem at  $t = 0.1$ .

### 3.1. Viscous shock tube problem

To evaluate the model’s ability in capturing HNE effects and its capacity in describing large-scale flow structures with steep macroscopic gradients, we compare the second-order DBM simulation results with Riemann solutions for various one-dimensional viscous shock tube problems.

#### 3.1.1. Sod shock tube

The Sod shock tube problem (Sod 1978), known for its rich characteristic structures, is commonly used to validate the effectiveness of fluid models. The initial conditions for the left and right sides of the shock tube are as follows:

$$\begin{cases} (\rho, u_x, u_y, T)|_L = (1.0, 0.0, 0.0, 1.0), \\ (\rho, u_x, u_y, T)|_R = (0.125, 0.0, 0.0, 0.8), \end{cases} \quad (3.3)$$

where subscripts “ $L$ ” and “ $R$ ” denote the macroscopic variables on the left and right sides of the discontinuity, respectively. The simulation parameters are  $c = 1.0$ ,  $\eta_0 = 1.0$ ; for  $1 \leq i \leq 4$ ,  $\eta_{ji} = i\eta_0$ ; for  $13 \leq i \leq 16$ ,  $\eta_{ji} = \eta_0$ ; otherwise,  $\eta_{ji} = 0$ , with  $j = 1, 2, 3$ . The spatial steps are  $\Delta x = \Delta y = 10^{-3}$ , and the time step is  $\Delta t = 2\tau = 10^{-4}$ . Additional parameters include  $\gamma = 1.4$  and  $\text{Pr} = 2.0$ , with the grid size being  $N_x = N_y = 1000 \times 2$ . Fixed boundary conditions are imposed in the  $x$ -direction, and periodic boundary conditions are applied in the  $y$ -direction. Figure 3 compares DBM results with Riemann solutions

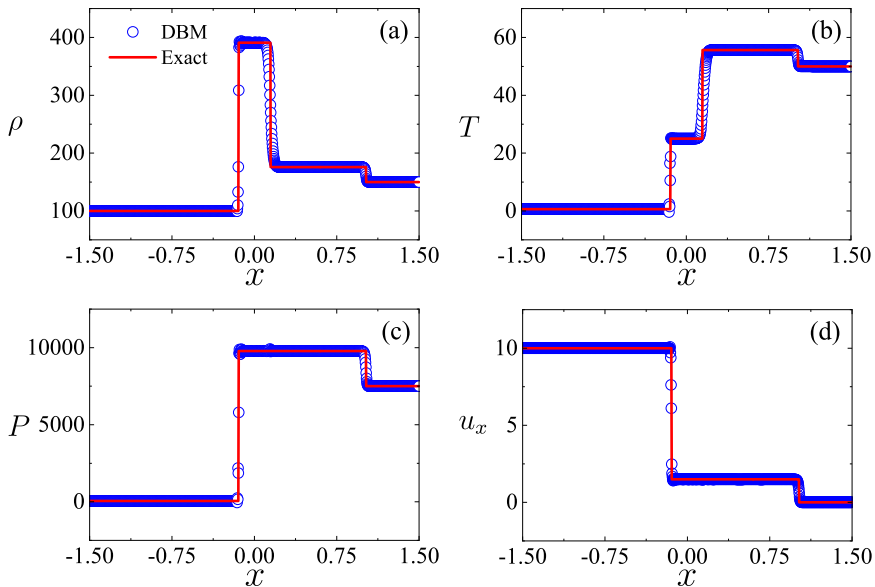


Figure 4: Comparison of DBM simulation results with Riemann solutions for the Mach 10 shock tube problem at  $t = 0.1$ .

for density (a), temperature (b), pressure (c), and velocity (d) at  $t = 0.1$ . The DBM effectively captures key structures, including rarefaction waves, contact discontinuities, and shock waves, while significantly reducing numerical dissipation. The DBM results are in good agreement with the Riemann solutions.

### 3.1.2. Mach 10 shock tube

Next, a shock tube problem with a large temperature gradient and an initial Mach number of 10 is used to validate the model. The initial conditions are

$$\begin{cases} (\rho, u_x, u_y, T)|_L = (100.0, 10.0, 0.0, 0.6), \\ (\rho, u_x, u_y, T)|_R = (150.0, 0.0, 0.0, 50.0). \end{cases} \quad (3.4)$$

The simulation parameters are as follows:  $c = 8.0$ ,  $\eta_0 = 40.0$ ; for  $1 \leq i \leq 4$ ,  $\eta_{1i} = i\eta_0$ , and for  $13 \leq i \leq 16$ ,  $\eta_{1i} = \eta_0$ ; otherwise,  $\eta_i = 0$ .  $\Delta x = \Delta y = 3 \times 10^{-3}$ ,  $\Delta t = 2\tau = 10^{-4}$ ,  $\gamma = 5/3$  and  $\text{Pr} = 2.0$ . The simulation results at  $t = 0.1$  are shown in figure 4. The DBM numerical solutions closely match the Riemann solutions, clearly capturing both the shock waves propagating both left and right, as well as the contact discontinuity. Using the Rankine-Hugoniot relations, the propagation speeds of the left and right shock waves are calculated as  $u_L = -1.442$  and  $u_R = 10.189$ , respectively. The DBM simulation gives the following results:  $u_L = -1.439$  for the left shock wave and  $u_R = 10.157$  for the right shock wave. The relative differences in propagation velocity for the left and right shock waves are only 0.21% and 0.31%, respectively. The primary reason for these

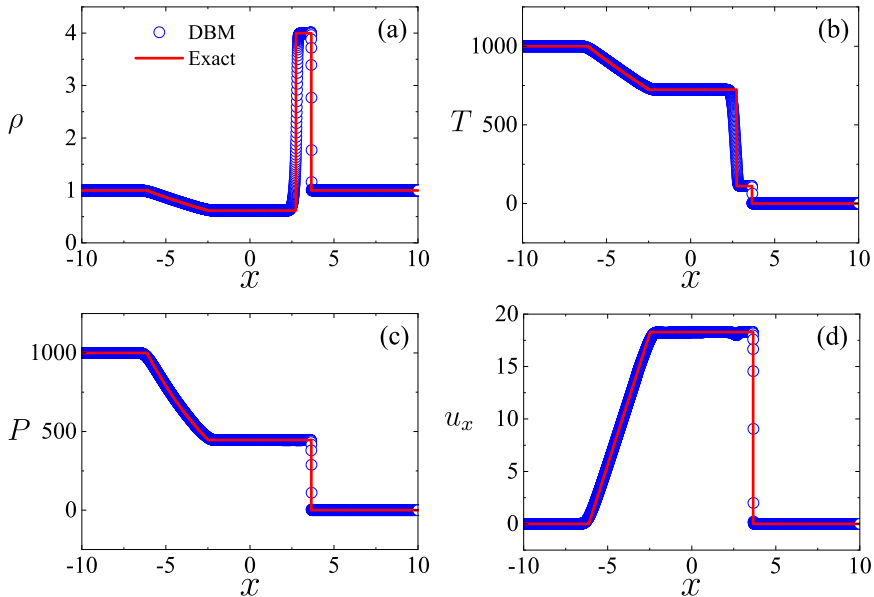


Figure 5: Comparison of DBM simulation results with Riemann solutions for Colella's explosion wave problem at  $t = 0.15$ .

discrepancies is that the DBM accounts for TNE effects, whereas the Riemann solution does not. Viscous dissipation and heat flux reduce the shock wave propagation speed and broaden the shock interface, which are not considered in the Riemann analytical solution.

### 3.1.3. Colella's explosion wave problem

An explosion wave is a pressure wave generated by the rapid release of a large amount of energy, with significant applications in defense engineering, astrophysics, and civil safety. A typical example of this phenomenon is Colella's explosion wave problem (Woodward & Colella 1984), which serves as a classic test case characterized by extreme temperature and pressure ratios, as well as high Mach numbers. The initial conditions for the problem are

$$\begin{cases} (\rho, u_x, u_y, T)|_L = (1.0, 0.0, 0.0, 1000.0), \\ (\rho, u_x, u_y, T)|_R = (1.0, 0.0, 0.0, 0.01). \end{cases} \quad (3.5)$$

The model and simulation parameters are  $c = 18.0$ ,  $\eta_0 = 40.0$ ; for  $1 \leq i \leq 4$ ,  $\eta_{1i} = i\eta_0$ , and for  $13 \leq i \leq 16$ ,  $\eta_{1i} = \eta_0$ ; otherwise,  $\eta_i = 0$ .  $\Delta x = \Delta y = 5 \times 10^{-3}$ ,  $\tau = 2\Delta t = 10^{-4}$ ,  $\gamma = 5/3$ ,  $\text{Pr} = 0.71$ . Figure 5 presents the simulation results at  $t = 0.15$ . The DBM numerical solution aligns well with the exact solution. The left-propagating rarefaction wave, the contact discontinuity, and the strong right-propagating shock wave are all accurately captured. The calculated Mach number of the rightward shock wave is  $Ma_{\text{DBM}} = 189.562$ , compared to  $Ma_{\text{RH}} = 189.002$  from the Rankine-Hugoniot relations.

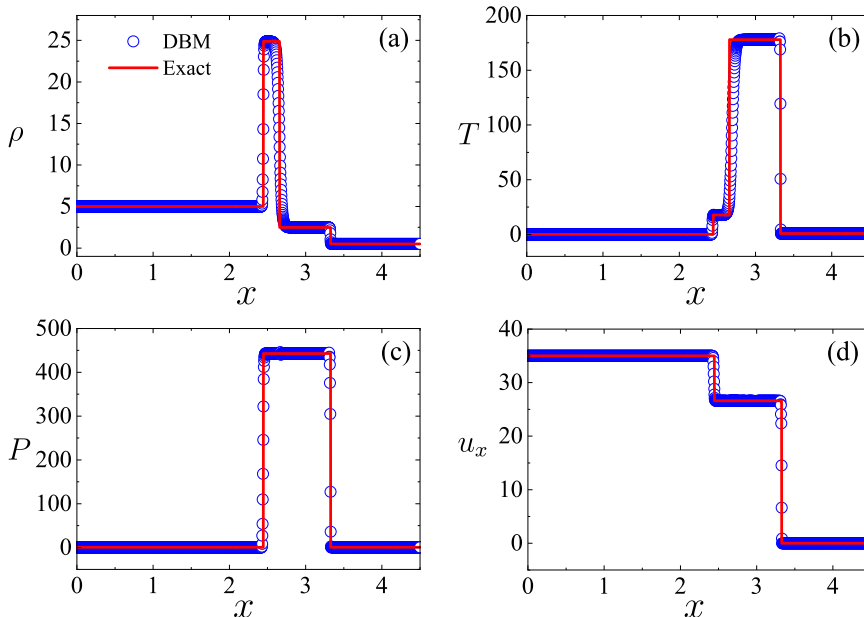


Figure 6: Comparison of DBM simulation results with Riemann solutions for the astrophysical jet problem at  $t = 0.1$ .

This negligible discrepancy is mainly due to the smaller relaxation time, which directly affects the intensity of TNE.

### 3.1.4. Astrophysical jet

Astrophysical jets are high-speed flows ejected from celestial bodies or interstellar matter. These jets play a significant role in influencing the interstellar medium, galaxy formation, and the dynamic evolution of the universe. The problem considered is a shock tube problem with large velocity gradients and multiple shock waves, characterized by high Mach numbers (Kallikounis *et al.* 2022; Reyhanian *et al.* 2023). It has important applications in areas such as vortex engines, rocket launches, rock explosions, and gas outbursts. The initial conditions are

$$\begin{cases} (\rho, u_x, u_y, T)|_L = (5.0, 35.0, 0.0, 0.08254) \\ (\rho, u_x, u_y, T)|_R = (0.5, 0.0, 0.0, 0.8254) \end{cases} \quad (3.6)$$

The model and simulation parameters are  $c = -14.0$ ,  $\eta_0 = 20.0$ ; for  $1 \leq i \leq 4$ ,  $\eta_{ji} = \eta_0$ , and for  $13 \leq i \leq 16$ ,  $\eta_{ji} = (i-12)\eta_0$  with  $j = 1, 2$ ; otherwise,  $\eta_i = 0$ .  $\Delta x = \Delta y = 3 \times 10^{-3}$ ,  $\tau = 3 \times 10^{-5}$ ,  $\Delta t = 5 \times 10^{-4}$ ,  $\gamma = 1.5$ . The simulation results at  $t = 0.1$  are shown in figure 6, demonstrating that the DBM solution agrees well with the exact solution. The two strong shock waves moving rightward, along with the contact discontinuity are clearly captured. The Rankine-Hugoniot relations yield  $Ma_1 = 64.0892$  for the first shock wave,

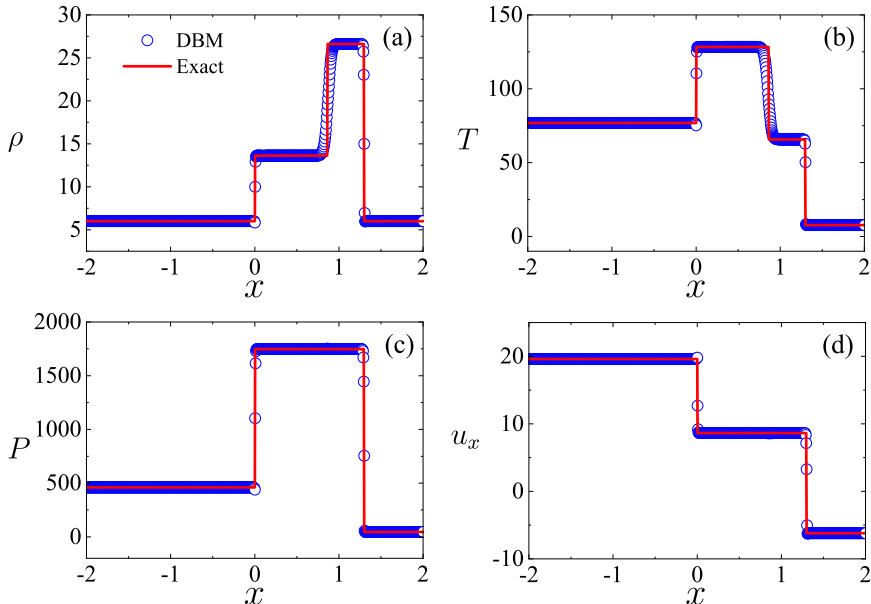


Figure 7: Comparison of DBM simulation results with Riemann solutions for the two strong shock collision problem at  $t = 0.1$ .

and  $Ma_2 = 30.286$  for the second shock wave. The DBM solution gives  $Ma_1 = 63.4475$  for the first shock wave, and  $Ma_2 = 30.4059$  for the second shock wave.

### 3.1.5. Collision of two strong shock waves

The collision of strong shock waves is a critical problem in astrophysics, plasma physics, explosion physics, and gas dynamics (Gan *et al.* 2008). Studying these collisions is crucial for understanding natural phenomena and engineering processes, such as supernova explosions, interactions between interstellar media, and inertial confinement fusion experiments. Additionally, applications such as high-energy particle experiments, vortex control, and jet engine design rely on the a deep understanding of these interactions. The initial conditions for this problem are:

$$\begin{cases} (\rho, u_x, u_y, T)|_L = (5.99924, 19.5975, 0, 76.82540) \\ (\rho, u_x, u_y, T)|_R = (5.99242, -6.19633, 0, 7.69222) \end{cases} \quad (3.7)$$

The model and simulation parameters are  $c = 9.0$ ,  $\eta_0 = 20.0$ . When  $1 \leq i \leq 4$ ,  $\eta_{1i} = \eta_{2i} = \eta_0$ , and when  $13 \leq i \leq 16$ ,  $\eta_{1i} = \eta_{2i} = i\eta_0$ ; otherwise,  $\eta_i = 0$ .  $\Delta x = \Delta y = 5 \times 10^{-3}$ ,  $\Delta t = 10\tau = 10^{-4}$ ,  $\gamma = 1.5$ ,  $\text{Pr} = 0.5$ . The simulation results at  $t = 0.1$  are presented in figure 7. The two strong shock waves propagating to the left and right, as well as the contact discontinuity, are accurately captured. The shock interfaces are sharp, with

no numerical oscillations. This demonstrates that DBM effectively handles the complex dynamics of strong shock wave collisions.

### 3.2. Simulation and analysis of thermodynamic nonequilibrium effects at different orders

The nonequilibrium behaviors in compressible flow systems are inherently complex and multifaceted. Traditional fluid mechanics employs parameters such as the Knudsen number (Kn), Mach number (Ma), Reynolds number (Re), viscosity, thermal conductivity, and macroscopic gradients to characterize deviations from equilibrium. These parameters provide a coarse-grained, condensed, and averaged representation of nonequilibrium effects from specific perspectives. However, detailed information about nonequilibrium states, such as internal energy distribution across different degrees of freedom, viscous stresses, heat fluxes, fluxes of these quantities, higher-order non-conserved moments, and their independent components, remains inaccessible and cannot be directly analyzed using traditional metrics. To address this limitation, a more comprehensive, multi-perspective, and finer-grained approach is required to study nonequilibrium effects in compressible flow systems, complementing the conventional descriptions provided by traditional fluid mechanics. The DBM utilizes the nonequilibrium intensity vector,  $\mathbf{S}_{\text{TNE}}$ , to realize a multi-perspective description of the nonequilibrium states and effects. Among the components of  $\mathbf{S}_{\text{TNE}}$ , viscous stress and heat flux, as key TNE measures in macroscopic fluid dynamics equations, directly influence the direction and mode of system evolution, necessitating detailed investigation. The following section will validate DBM's ability to describe viscous stress and heat flux across scales using specific examples.

#### 3.2.1. Typical thermodynamic nonequilibrium quantity: Viscous Stress

Fluid collision problems involve interactions, intersections, or collisions between two or more fluids. At collision points or regions, intense fluid interactions give rise to pronounced local HNE and TNE effects. These effects manifest as abrupt macroscopic gradient shifts, sharp increases in viscous stress and/or heat flux, and the emergence of multiscale phenomena. Investigating the multiscale behaviors and nonequilibrium effects in fluid collisions is crucial for advancing our understanding of fluid dynamics, mixing processes, and material exchange.

For the problem considered, the initial conditions are:

$$\rho(x, y) = \frac{\rho_L + \rho_R}{2} - \frac{\rho_L - \rho_R}{2} \tanh\left(\frac{x - N_x \Delta x / 2}{L_\rho}\right), \quad (3.8)$$

$$u_x(x, y) = -u_0 \tanh\left(\frac{x - N_x \Delta x / 2}{L_u}\right). \quad (3.9)$$

For cases I-III in Table 1, the pressure is uniform  $P_L = P_R = P_0$ ,  $T(x, y) = P_0 / \rho(x, y)$ . For case IV, the temperature is defined as  $T(x, y) = \frac{T_L + T_R}{2} - \frac{T_L - T_R}{2} \tanh\left(\frac{x - N_x \Delta x / 2}{L_T}\right)$ .

Table 1: Physical parameters for cases with different orders of viscous stress.

Case	$\Delta_{2xx}^*$	Density	Temperature	Velocity	Relaxation time	Pr
I	weak	$\rho_L = 2\rho_R = 2$	$2T_L = T_R = 2$	$u_0 = 0.0$	$3 \times 10^{-4}$	0.71
II	moderate	$\rho_L = 2\rho_R = 2$	$2T_L = T_R = 2$	$u_0 = 0.3$	$3 \times 10^{-4}$	0.71
III	strong	$\rho_L = 2\rho_R = 2$	$2T_L = T_R = 2$	$u_0 = 1.0$	$2 \times 10^{-3}$	0.71
IV	super-strong	$10^{12}\rho_L = \rho_R = 10^6$	$2T_L = T_R = 2$	$u_0 = 0.3$	$3 \times 10^{-3}$	0.71

For all cases,  $u_y(x, y) = 0$ . Here,  $\rho_L$ ,  $T_L$ ,  $P_L$  are the macroscopic quantities on the left side, while  $\rho_R$ ,  $T_R$ ,  $P_R$  are those on the right side of the fluids.  $L_\rho$ ,  $L_T$ , and  $L_u$  represent the interface widths for density, temperature and velocity, respectively.  $u_0$  is a free variable controlling the strength of the collision. The other parameters are set as  $\Delta x = \Delta y = 1.5 \times 10^{-3}$ ,  $\Delta t = 5 \times 10^{-5}$ ,  $c = 1.0$ ,  $\eta_0 = 6.0$ , and  $\gamma = 5/3$ .

In an ideal gas system, the TNE behavior is governed by the relaxation time  $\tau$ , as well as the macroscopic quantities and their gradients. Consequently, we define a five-component vector,  $\mathbf{S}_{\text{TNE}} = (\tau, \nabla \rho, \nabla T, \nabla \mathbf{u}, \Delta_2^*)$  to evaluate the system's nonequilibrium effects. By adjusting these parameters, multiscale flows with varying nonequilibrium intensities and Knudsen numbers can be generated.

Figure 8 compares the numerical solutions of viscous stress obtained from the first-order DBM (left column) and the second-order DBM (right column) under four different TNE intensities. The results for the first three cases are taken at  $t = 0.025$ , while the final case is taken at  $t = 0.015$ . In each panel, the analytical solutions with first- and second-order accuracies, calculated from equations 2.9 and A 1, are shown as dashed and solid lines, respectively. As shown in the first row of figure 8, a smaller relaxation time  $\tau$  and negligible velocity gradient  $\nabla \mathbf{u}$  lead to weaker TNE effects. At the beginning of the evolution, where there are no velocity gradients ( $u_0(x, y) = 0$ ), the viscous stress is driven by density and temperature gradients rather than velocity gradients, as indicated by equation A 1, resulting in  $\Delta_{2xx}^{*(2)} > \Delta_{2xx}^{*(1)} \approx 0$ . Subsequently, the density and temperature gradient terms in equation A 1 gradually induce velocity gradients in equation 2.9, i.e., the second-order TNE effects trigger the first-order TNE effects. As the system evolves,  $\Delta_{2xx}^{*(1)}$  surpasses  $\Delta_{2xx}^{*(2)}$  and becomes the dominant factor in the evolution. Figure 8(a) demonstrates that, even in weak nonequilibrium scenarios, the NS-level DBM, which neglects second-order TNE effects, exhibits significant deviations between its analytical and numerical solutions. In contrast, the Burnett-level DBM, which accounts for second-order TNE effects, shows good agreement between analytical and numerical results, providing a more comprehensive description of weak nonequilibrium effects.

Increasing the collision velocity  $u_0$  strengthens the TNE effects, resulting in moderate



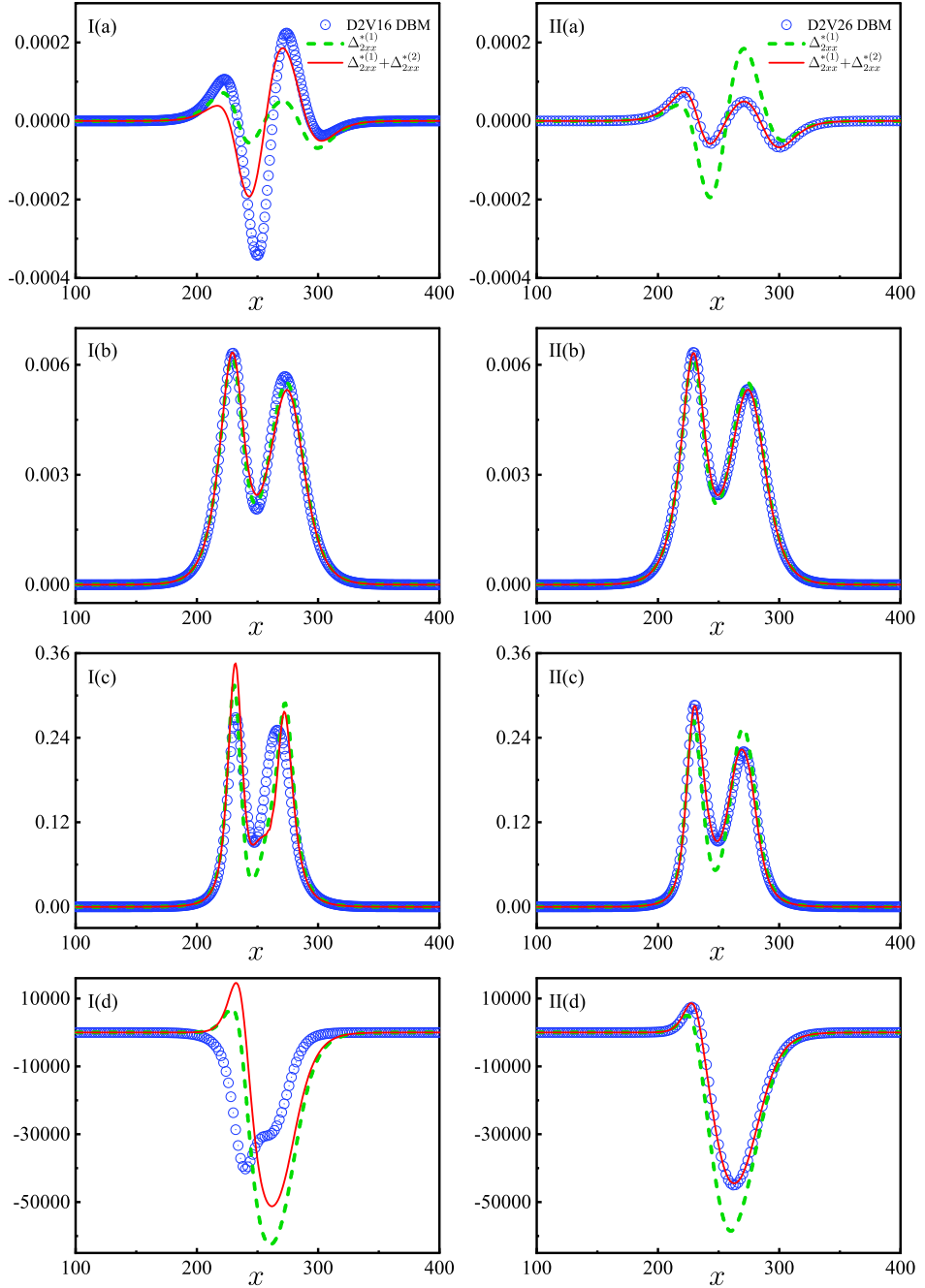


Figure 8: Comparison of numerical solutions for viscous stress calculated using the first-order DBM (left column) and the second-order DBM (right column), for weak, moderate, strong, and super-strong TNE cases, where dashed and solid lines represent the analytical solutions with first- and second-order accuracies, respectively.

viscous stress (second row of figure 8). At this stage,  $\Delta_{2xx}^{(1)}$  is approximately 30 times larger than in the case of weak TNE intensity. Importantly,  $\Delta_{2xx}^{(2)}$  can be neglected compared to  $\Delta_{2xx}^{*(1)}$ , indicating that velocity gradients dominate the driving forces of TNE, rather than density and temperature gradients. Both the second-order DBM (D2V26 model) and the first-order DBM (D2V16 model) effectively describe TNE effects under this condition, although the second-order model provides better accuracy.

By further increasing  $\tau$  and  $u_0$ , the TNE intensity is significantly elevated to a strong level, as illustrated in the third row of figure 8. Compared with the D2V16 model, the simulation results of the D2V26 model consistently aligns with the second-order analytical solution, highlighting the effectiveness and necessity of the second-order model under strong nonequilibrium conditions. Moreover, in this scenario, at the left peak,  $|\Delta_{2xx}^{*(1)}| \approx |\Delta_{2xx}^{*(1)} + \Delta_{2xx}^{*(2)}|$ , indicating that the second-order TNE exerts zero feedback on the first-order nonequilibrium. In the center of the computational domain,  $|\Delta_{2xx}^{*(1)}| > |\Delta_{2xx}^{*(1)} + \Delta_{2xx}^{*(2)}|$ , suggesting that second-order TNE provides negative feedback to first-order TNE. At the right peak,  $|\Delta_{2xx}^{*(1)}| < |\Delta_{2xx}^{*(1)} + \Delta_{2xx}^{*(2)}|$ , indicating that the second-order TNE contributes positive feedback to the first-order TNE. It is evident that higher-order TNE exhibits complex feedback effects on lower-order TNE. The specific nature of the feedback depends on the local flow states.

When the density ratio is further increased to  $10^{12}$  and  $\tau$  is raised to  $3 \times 10^{-3}$ , the amplitude of  $\Delta_{2xx}^*$  rapidly increases to the order of  $10^4$  [fourth row of figure 8]. At this point, the numerical solution of the D2V16 model deviates significantly from both the first-order and second-order analytical solutions. The numerical solution of the D2V26 model still perfectly matches the second-order analytical solution, but significantly deviates from the first-order one due to the contribution of the density gradient terms in equation A 1.

Figure 10(a) illustrates the distributions of the Knudsen number  $Kn$  calculated from gradients of macroscopic quantities in the case of super-strong nonequilibrium. The Knudsen number is defined as  $Kn = \lambda/L$ , where  $\lambda = c_s\tau$  represents the molecular mean-free-path and  $L = \phi/|\nabla\phi|$  is a local characteristic length scale,  $c_s = \sqrt{\gamma T}$  is the local speed of sound, and  $\phi$  signifies the macroscopic quantity. Notably, the maximum Knudsen number  $Kn_{\max}$  exceeds 0.3, which is far beyond the applicability of the NS model. In other words, the D2V26 model is applicable for studying flow problems in the early transition flow regime.

From figure 8, we conclude that whether or not to consider the higher-order TNE effects depends on their relative importance compared to lower-order TNE effects, or the discrepancies between analytical solutions of different orders, rather than solely on the Knudsen number. For example, second-order TNE effects should be considered in

Table 2: Physical parameters for cases with different orders of heat flux.

Case	$\Delta_{3,1x}^*$	Density	Temperature	Velocity	Relaxation time	Pr
	weak					
I-III	moderate	$2\rho_L = \rho_R = 2$	$T_L = T_R = 1.5$	$u_{xL} = 0.2$ $u_{xR} = 0$	$2 \times 10^{-3}$	0.3
	strong					
IV	super-strong	$10^{12}\rho_L = \rho_R = 10^6$	$2T_L = T_R = 2$	$u_{xL} = 0.5$ $u_{xR} = 0$	$2.5 \times 10^{-3}$	0.6

rows 1, 3, and 4, even though the maximum local Knudsen numbers for the weak and strong nonequilibrium cases are only  $5.18 \times 10^{-3}$  and 0.09, respectively. Therefore, the relative nonequilibrium intensity is used to measure the relative importance of higher-order nonequilibrium effects, defined as  $R_{\text{TNE}} = |\Delta_{m,n}^{*(j+n)} / \Delta_{m,n}^{(j)}|$ . In the scenarios shown in rows 1, 3, and 4, the maximum relative nonequilibrium intensities  $R_{\text{TNE-max}} = \Delta_{2,xx}^{*(2)} / \Delta_{2,xx}^{*(1)}$  are 0.73, 0.78, and 0.24, respectively. This approach provides a more reasonable method for describing the multiscale characteristics under investigation and for determining the appropriate model order in physical modeling.

### 3.2.2. Typical thermodynamic nonequilibrium quantity: Heat Flux

Next, the model's ability to describe multiscale heat flux is examined similarly. The initial conditions are given by

$$\phi(x, y) = \frac{\phi_L + \phi_R}{2} - \frac{\phi_L - \phi_R}{2} \tanh\left(\frac{x - N_x \Delta x / 2}{L_\phi}\right), \quad (3.10)$$

where  $\phi = [\rho, T, u_x]$ . Table 2 lists the initial macroscopic parameters on the left and right sides of the system for four cases. Figure 9 compares the numerical solutions from the first-order DBM (left column) and second-order DBM (right column) across four levels of nonequilibrium intensity, along with corresponding analytical solutions for both orders.

The first three rows of figure 9 depict weak, strong, and moderate nonequilibrium cases at  $t = 0.0175, 0.025,$  and  $0.5$ , representing distinct stages of the evolution process. Initially, in the absence of a temperature gradient ( $T_L = T_R = 1.5$ ), the heat flux is primarily driven by density and velocity gradients, as described in equation (A 4). This results in  $\Delta_{3,1x}^{(2)} > \Delta_{3,1x}^{(1)} \approx 0$ . Subsequently, the density and velocity gradients gradually induce temperature gradients, leading to  $\Delta_{3,1x}^{*(1)}$  surpassing  $\Delta_{3,1x}^{*(2)}$ , as shown in the second and third rows of figure 9. Specifically, in panel IIC,  $\Delta_{3,1x}^{*(2)}$  becomes negligible relative to  $\Delta_{3,1x}^{*(1)}$  as the density and velocity gradients diminish. These findings demonstrate that in an evolving nonequilibrium system, the nonequilibrium intensity varies substantially across different stages. Initially, one or more nonequilibrium driving

forces initiate additional types of nonequilibrium effects, which at a certain point cause the nonequilibrium effects to peak, forming distinct multiscale structures within the system. As the system evolves, macroscopic quantities become more uniform, and the nonequilibrium driving forces weaken due to dissipation, leading to a simplified and stable flow structure. As a multiscale model, it should adapt to capture cross-scale nonequilibrium effects. The results of the D2V26 model, displayed in the right column of figure 9, precisely exemplify this capability.

When further increasing the density, temperature, and velocity gradients, along with relaxation time, the heat flux transitions into the super-strong regime, as depicted in the fourth row of figure 9. At this stage, the low-order model fails to adequately capture such intense nonequilibrium effects, whereas the second-order model's numerical solution still matches the second-order analytical solution.

Additionally, as illustrated in figure 10(b), the maximum Knudsen number, derived from gradients of macroscopic quantities in the super-strong nonequilibrium case, exceeds 0.25. interactions and intensified nonequilibrium forces that emerge in the super-strong regime, providing a more physical description of the system's evolving heat flux. This observation underscores the superior capability of the second-order model to address the complex multiscale interactions and intensified nonequilibrium forces characteristic of the super-strong regime, thereby providing a more accurate and comprehensive description of the system's evolving heat flux.

From the above analysis of a multiscale nonequilibrium flow problem, the following conclusions can be drawn: (1) The first-order model overestimates nonequilibrium effects under both weak and strong nonequilibrium conditions; (2) The D2V26 model, which satisfies more kinetic moment relations and provides a comprehensive description of first- and second-order TNE, accurately predicts nonequilibrium effects consistent with analytical solutions in the three analyzed scenarios. This highlights its multiscale capability in describing nonequilibrium phenomena. (3) In nonequilibrium flows, the consideration of which-order nonequilibrium effects to include in physical modeling depends on the relative nonequilibrium intensity rather than the Knudsen number; (4) In most cases shown in the figure, second-order nonequilibrium effects oppose first-order effects, resulting in a negative feedback.

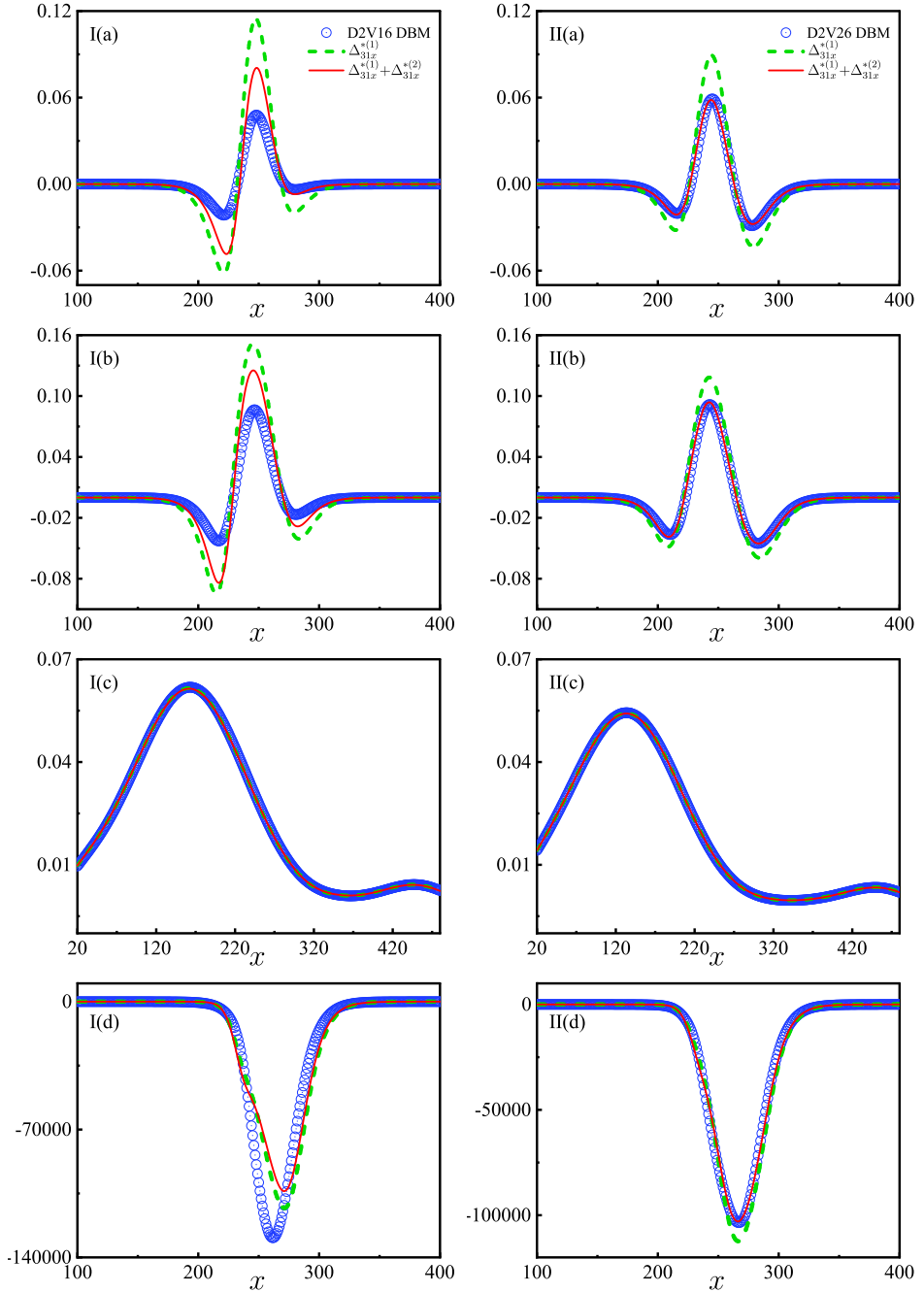


Figure 9: Comparison of numerical solutions for heat flux calculated using the first-order DBM (left column) and the second-order DBM (right column) under weak, moderate, strong, and super-strong TNE cases, where dashed and solid lines represent the analytical solutions with first- and second-order accuracies, respectively.

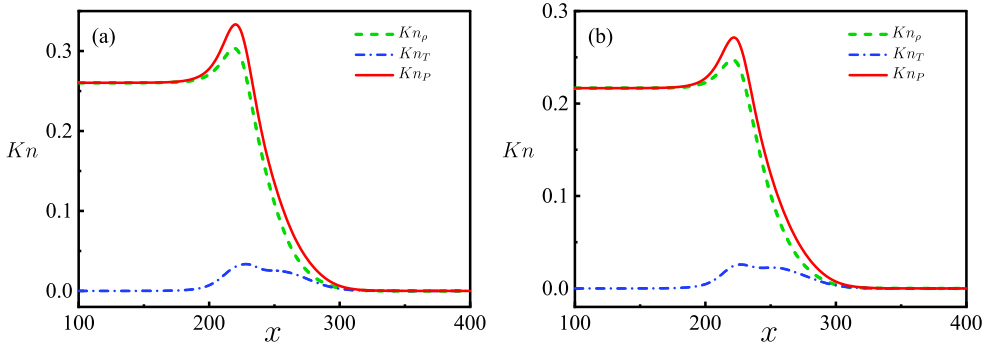


Figure 10: Distributions of the Knudsen number calculated from gradients of macroscopic quantities in the super-strong viscous stress (a) and heat flux (b) cases.

#### 4. Thermodynamic nonequilibrium effects and entropy production mechanisms in the regular reflection of shock wave

This section investigates the TNE effects and entropy production mechanisms in regular shock wave reflection, which are crucial for understanding the complex flow dynamics and wave structures in a supersonic inlet.

The supersonic inlet of a scramjet engine, a vital aerodynamic component, exhibits flow phenomena including oblique shocks induced by the inlet compression angle, boundary layers generated by flow-wall interactions, separation bubbles caused by reflected shock-boundary layer interactions, reflected shocks near the inlet lip, and expansion waves at corners (Li & Ben-Dor 1997; Huang *et al.* 2020; Chang *et al.* 2017; Qiu *et al.* 2017; Bao *et al.* 2022). These phenomena collectively increase aerodynamic drag, reduce air mass flow rate, and decrease inlet efficiency, ultimately impacting the engine's stability, reliability, and overall performance.

TNE effects and entropy production mechanisms play a vital role in governing interactions among shocks, boundary layers, and separation bubbles. Shock wave reflection, in particular, significantly influences wave drag and frictional drag, which are the main contributors to the inlet's total aerodynamic drag. Analyzing the thermodynamic properties and flow dynamics of shock wave reflection reveals mechanisms underlying performance losses and aids in developing strategies to minimize drag, ultimately enhancing thrust and combustion efficiency in supersonic engines.

Li *et al.* investigate the transition from regular reflection to Mach reflection in steady supersonic flow, caused by an upstream disturbance (Li *et al.* 2011). Through computational fluid dynamics simulation, they observe multiple shock interactions in the early stage, including a triple-shock structure and shock/slipline interaction. Yao *et al.* address shock reflection in supersonic and hypersonic intake flow under off-design conditions (Yao

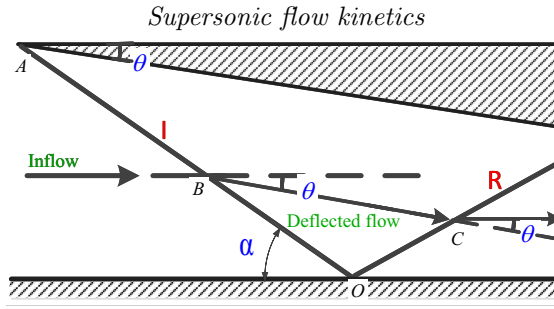


Figure 11: Schematic diagram of the regular shock wave reflection.

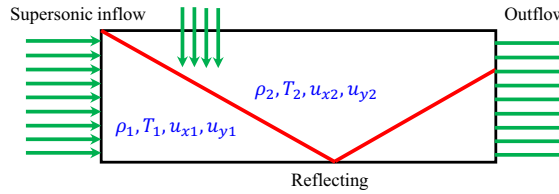


Figure 12: Boundary condition settings for regular shock wave reflection.

*et al.* 2013). They focus on the interaction between the incident shock wave, an upstream expansion wave generated by the lip, and the downstream shock wave interacting with a cowl-turning deflected shock wave. The study also analyzes the influence of the lip and cowl turning angles on the flow structure and the transition between regular and Mach reflection. The findings suggest that the interference between the expansion and shock waves significantly alters the dual-solution domain, with the Mach stem height increasing with the turning angle.

As research progresses, an increasing number of studies focus on the nonequilibrium effects in shock reflection, such as viscosity, heat conduction, and rarefaction effects. Khotyanovsky *et al.* investigate the viscous effects in steady shock wave reflection for a Mach 4 flow of a monatomic gas, using both NS and DSMC simulations (Khotyanovsky *et al.* 2009). They focus on the impact of viscosity and heat conduction near the shock intersection, where flow parameters deviate from inviscid predictions. The study highlights the discrepancies caused by viscous and heat transfer effects, which are significant in high-speed aerodynamics, particularly during shock interactions in supersonic and hypersonic flows. Shoen *et al.* explore the effects of viscosity and rarefaction on regular shock wave reflections (Shoen *et al.* 2017). They highlight that traditional Rankine-Hugoniot relations describe flow parameters behind shock waves but do not provide information on the internal structure of the shock wave itself. For regular shock reflection in a viscous gas, they present an analytical solution in the vicinity of the reflection point. This solution consists of three zones with constant parameters, separated by infinitely thin discontinuity lines (incident and reflected shock waves). In the case of a viscous

gas, the shock waves have finite thickness, and the viscous effects must be considered. Timokhin *et al.* extend the classical Mott-Smith solution for one-dimensional normal shock wave structure to the two-dimensional regular shock reflection problem (Timokhin *et al.* 2022). The solution is expressed in terms of a nonequilibrium molecular velocity distribution function along the symmetry-plane streamline, represented as a weighted sum of four Maxwellians. The applicability of the solution is analyzed using DSMC simulations across a range of incident shock wave intensities. The results show that the accuracy of the solution improves with increasing Mach number, and becomes especially accurate for strong shocks where  $Ma > 8$ . Qiu and Bao *et al.* study the nonequilibrium characteristics during the development of regular reflections of shock wave (Qiu *et al.* 2017, 2020; Bao *et al.* 2022; Qiu *et al.* 2024). They point out that the nonequilibrium kinetic moments related to mass can be used to determine the position of boundary layer separation, while nonequilibrium kinetic moments related energy determine the total energy variation inside the boundary layer (Bao *et al.* 2022). However, the nonequilibrium effects in the regular reflection process are rich and complex. Viscosity and heat conduction alone are insufficient to capture their intricate characteristics. Therefore, in this section, we use the nonequilibrium intensity vector,  $\mathbf{S}_{\text{TNE}}$ , defined by DBM to meticulously describe the discrete/non-equilibrium states, effects, and behaviors during the shock reflection process.

Figure 11 shows a schematic diagram of the two-dimensional regular shock wave reflection flow field. An inclined wedge with an angle of  $\theta$  is positioned at the upper section of the flow field. The incoming flow with a high  $Ma$  propagates from left to right, forming an oblique shock with an incident angle of  $\alpha$  under the influence of the wedge. When the incident angle is small enough, the shock reflects off the lower wall and a reflected shock is formed, dividing the region between the wedge and the lower wall into three parts. The two sides of the incident shock wave (region 1 and 2) satisfy the following relationship

$$\begin{cases} \frac{\rho_2}{\rho_1} = \frac{(\gamma+1)M_1^2 \sin^2 \alpha}{2+(\gamma-1)M_1^2 \sin^2 \alpha} \\ \frac{p_2}{p_1} = \frac{2\gamma M_1^2 \sin^2 \alpha - (\gamma-1)}{\gamma+1} \\ M_2^2 \sin^2(\alpha - \theta) = \frac{\gamma+1+(\gamma-1)(M_1^2 \sin^2 \alpha - 1)}{\gamma+1+2\gamma(M_1^2 \sin^2 \alpha - 1)} \\ \tan \theta = \tan \alpha \frac{M_1^2 \cos^2 \alpha - \cot^2 \alpha}{1 + \frac{1}{2}M_1^2(\gamma + \cos 2\alpha)} \end{cases} \quad (4.1)$$

Figure 12 depicts the boundary conditions applied in the simulation. The left boundary employs a supersonic inflow boundary condition, while the right boundary adopts an outflow boundary condition. The upper and lower boundaries adopt the Dirac and the specular reflection conditions, respectively. The Shakhov-BGK DBMs considering the 1st and 2nd orders of TNE are used for the simulation, respectively. The initial inflow is uniformly set as  $(\rho, T, u_x, u_y) = (\rho_0, T_0, Ma\sqrt{\gamma T_0}, 0.0)$ , with model parameters  $\tau = 10^{-3}$ ,



$\Delta x = \Delta y = 0.005$ ,  $c = 1.6$ . For  $1 \leq i \leq 4$ ,  $\eta_i = \eta_0 i$ , and for  $13 \leq i \leq 20$ ,  $\eta_i = 1.6$ , while in other cases  $\eta_i = 0.0$ .

#### 4.1. Necessity of high-order models: Ensuring positivity of entropy production

The origin of entropy production primarily stems from irreversible processes within the system. Using the DBM, entropy production rate due to both viscosity and heat flux can be obtained simultaneously. The total entropy production rate and the contributions from viscosity and heat flux are defined as follows:

$$\dot{S} = \frac{dS}{dt} = \int (\mathbf{\Delta}_{3,1}^* \cdot \nabla \frac{1}{T} - \frac{1}{T} \mathbf{\Delta}_2^* : \nabla \mathbf{u}) d\mathbf{r} \quad (4.2)$$

$$\dot{S}_{\text{NOMF}} = \frac{dS_{\text{NOMF}}}{dt} = - \int \frac{1}{T} \mathbf{\Delta}_2^* : \nabla \mathbf{u} d\mathbf{r} \quad (4.3)$$

$$\dot{S}_{\text{NOEF}} = \frac{dS_{\text{NOEF}}}{dt} = \int \mathbf{\Delta}_{3,1}^* \cdot \nabla \frac{1}{T} d\mathbf{r}. \quad (4.4)$$

When performing physical modeling, the accuracy of the required DBM depends on the specific nature of the problem and research requirements. In cases with weak nonequilibrium effects, a first-order DBM is sufficient to meet the physical requirements. However, with increased system discretization and nonequilibrium effects, higher-order DBMs that account for higher-order TNE effects can provide more reasonable results. In this study, the required order of DBM for studying shock-induced regular reflection is determined by examining the positivity of entropy production. Specifically, the initial conditions are set as  $(\rho, T, u_x, u_y) = (1.0, 1.0, 2.2\sqrt{1.4}, 0.0)$ .

Figure 18 shows entropy production rates using first-order (a) and second-order (b) DBMs along  $y = 40\Delta y$  at  $t = 1.8$ , with lines in (b) showing second-order analytical solutions. It can be observed that, in (a), the curves for the three types of entropy production rates calculated from the first-order DBM exhibit significant numerical oscillations, including substantial negative values near the incident and reflected shocks. In contrast, in (b), the entropy production rate curves calculated from the second-order DBM are smooth, consistently positive, and closely match the second-order analytical solutions. This indicates that the second-order model, compared to the first-order model, more accurately represents viscous stress and heat flux, captures dissipative mechanisms precisely, ensures entropy production non-negativity in line with the second law of thermodynamics, and exhibits better numerical stability, making it more suitable for analyzing strong nonequilibrium flows.

*This demonstrates that, compared to the first-order model, the second-order model provides more accurate representations of viscous stress and heat flux, describes dissipative mechanisms more precisely, ensures the non-negativity of entropy production according*

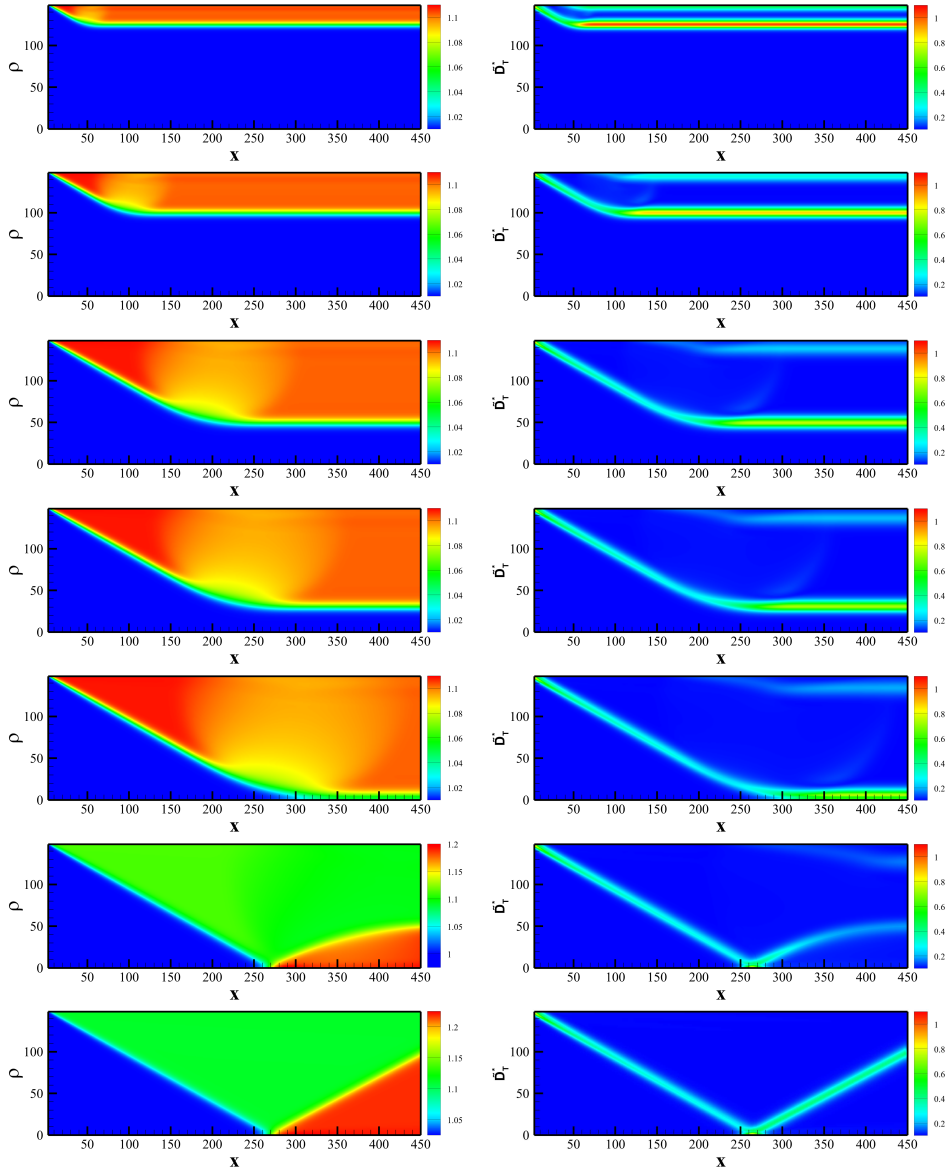


Figure 13: Density contours (left column) and nonequilibrium intensity contours (right column) at characteristic moments during the regular shock wave reflection process for  $Ma = 2.2$ . The corresponding moments, from top to bottom, are  $t = 0.1, 0.2, 0.4, 0.475, 0.575, 0.8, 1.8$ , respectively.

*to the second law of thermodynamics, and exhibits better numerical stability, making it more suitable for studying strong nonequilibrium flows.*

#### 4.2. Process of the regular reflection of shock wave

Depending on the incident angle, the reflection of an oblique shock on a plane can be categorized as regular reflection or Mach reflection. Figure 13 shows the density contours (left column) and nonequilibrium intensity contours (right column) at characteristic moments during the regular reflection process of a shock wave for  $Ma = 2.2$ . It can be seen that the regular reflection process can be divided into three stages: (1) When  $t < 0.575$ , the left-incoming flow is compressed by the upstream flow, forming a transient curved incident shock with positive curvature that gradually propagates downward. (2) At about  $t = 0.575$ , the incident shock strikes the lower wall and reflects, creating a curved reflected shock with negative curvature (Shi *et al.* 2020). During  $0.575 < t < 1.8$ , the curved reflected shock gradually straightens under the influence of the lower wall. (3) When  $t > 1.8$ , the reflected shock stabilizes, both the incident and reflected shocks become clearly distinguishable.

By measuring the incident or reflected shock angles, the model's ability to capture strong nonequilibrium shocks can be validated. When the regular reflection develops to a steady state, the incident angle of the shock simulated by BDM is  $29.1^\circ$  as shown in figure 13, with a relative error of 0.34% compared to the analytical value. This confirms the accuracy of the DBM in capturing the shock incident angle. As shown in the right column of figure 13, nonequilibrium effects are concentrated near the shock interfaces, while the rest of the flow field remains close to equilibrium. Additionally, the intensity of the reflected shock is slightly stronger than that of the incident shock, with an intensity ratio of approximately 1.41 at  $t = 1.8$ . This difference arises from the relatively lower Mach number of the upstream flow. By analyzing the nonequilibrium intensity, the positions and evolution characteristics of the incident and reflected shock waves can be effectively determined.

Figure 14 presents the steady-state distributions of density, temperature, pressure,  $x$ -velocity,  $y$ -velocity, and nonequilibrium intensity for the regular shock wave reflection at  $Ma = 2.2$  (left column) and  $Ma = 5.0$  (right column). When  $t > 1.8$ , the shock reflection process reaches a steady state. In both cases, the incident and reflected shocks divide the flow field into three regions, displaying no oscillations but maintaining a finite interface width. This suggests that the second-order model effectively captures large-scale flow structures in supersonic flows. Compared to the  $Ma = 2.2$  case, the shock interface in the  $Ma = 5.0$  case is significantly narrower, indicating an enhanced compressive effect on the airflow at higher Mach numbers. Furthermore, the total nonequilibrium strength in the  $Ma = 5.0$  case is much higher than in the  $Ma = 2.2$  case, with a ratio of approximately  $6 \times 10^2$ . This indicates that higher Mach numbers can rapidly increase the system's nonequilibrium strength.

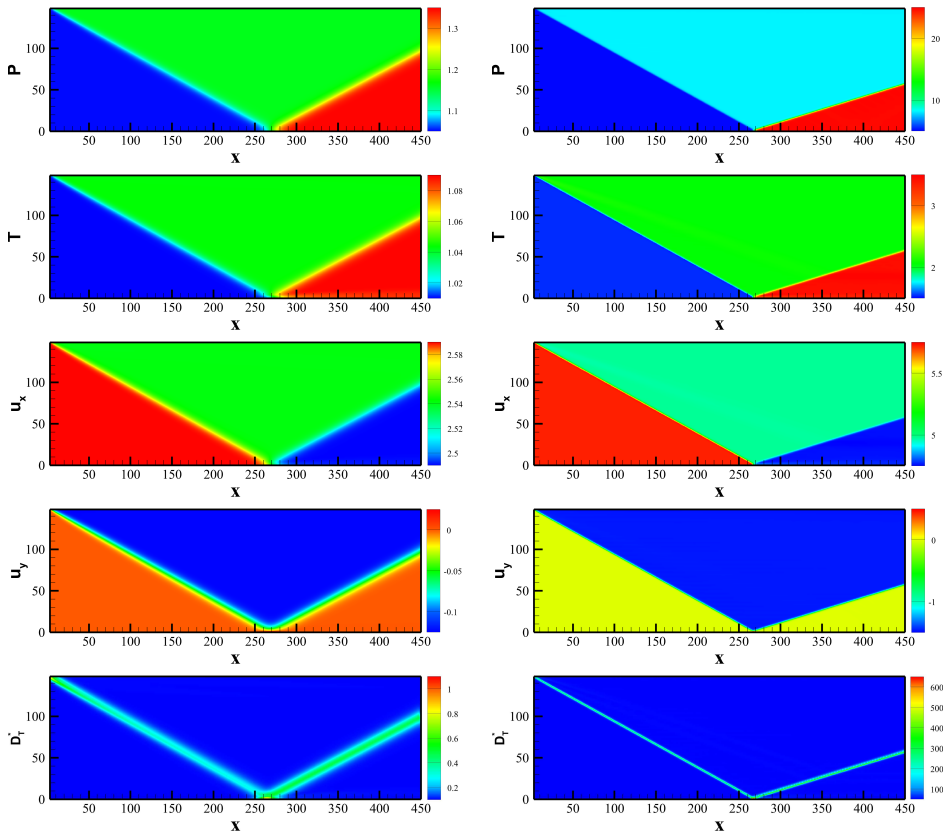


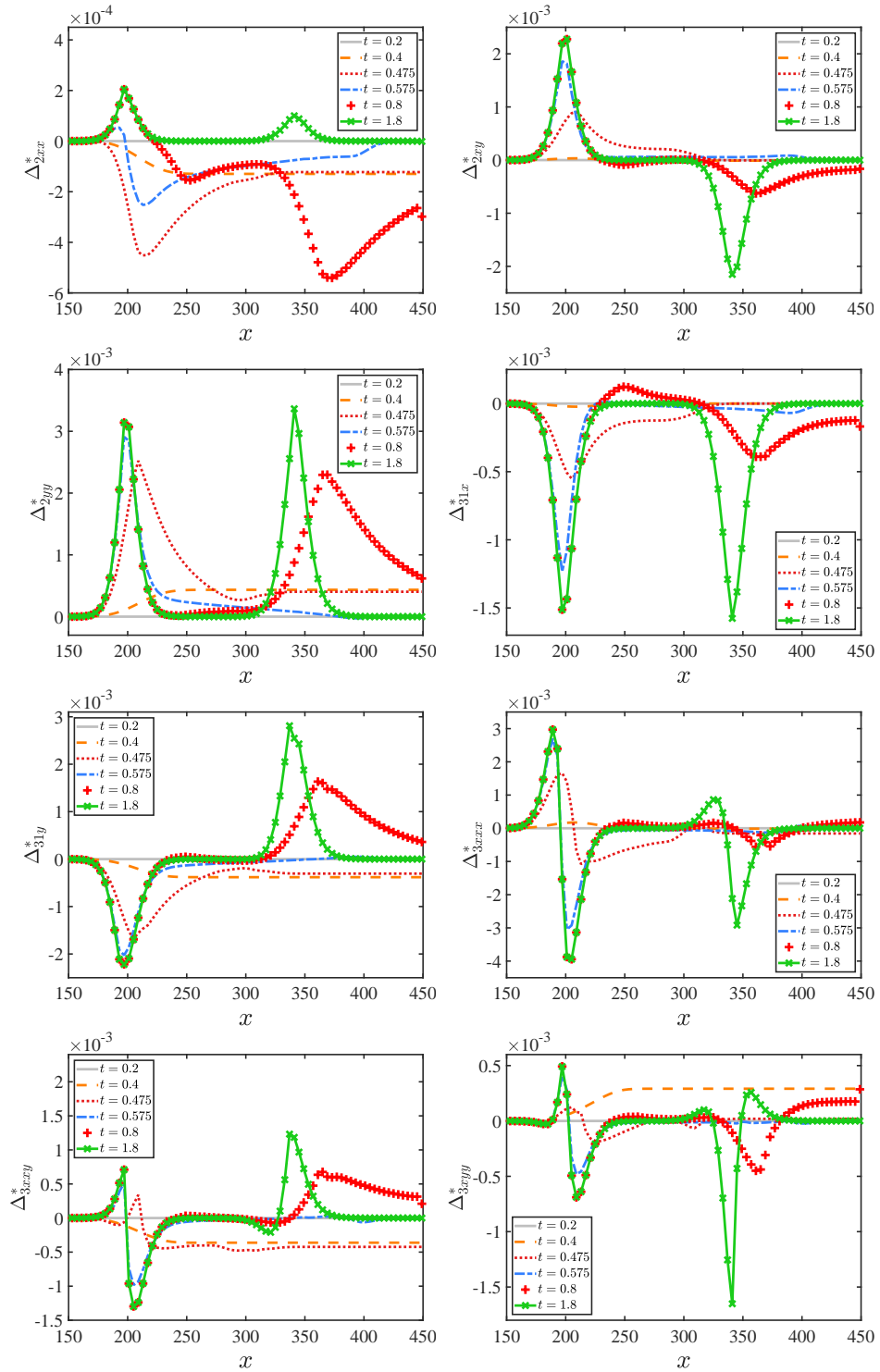
Figure 14: Density, temperature, pressure,  $x$ -velocity,  $y$ -velocity, and nonequilibrium intensity distributions at steady state for the regular shock wave reflection (left column:  $Ma = 2.2$ , right column:  $Ma = 5.0$ ).

### 4.3. Evolution of thermodynamic nonequilibrium quantities

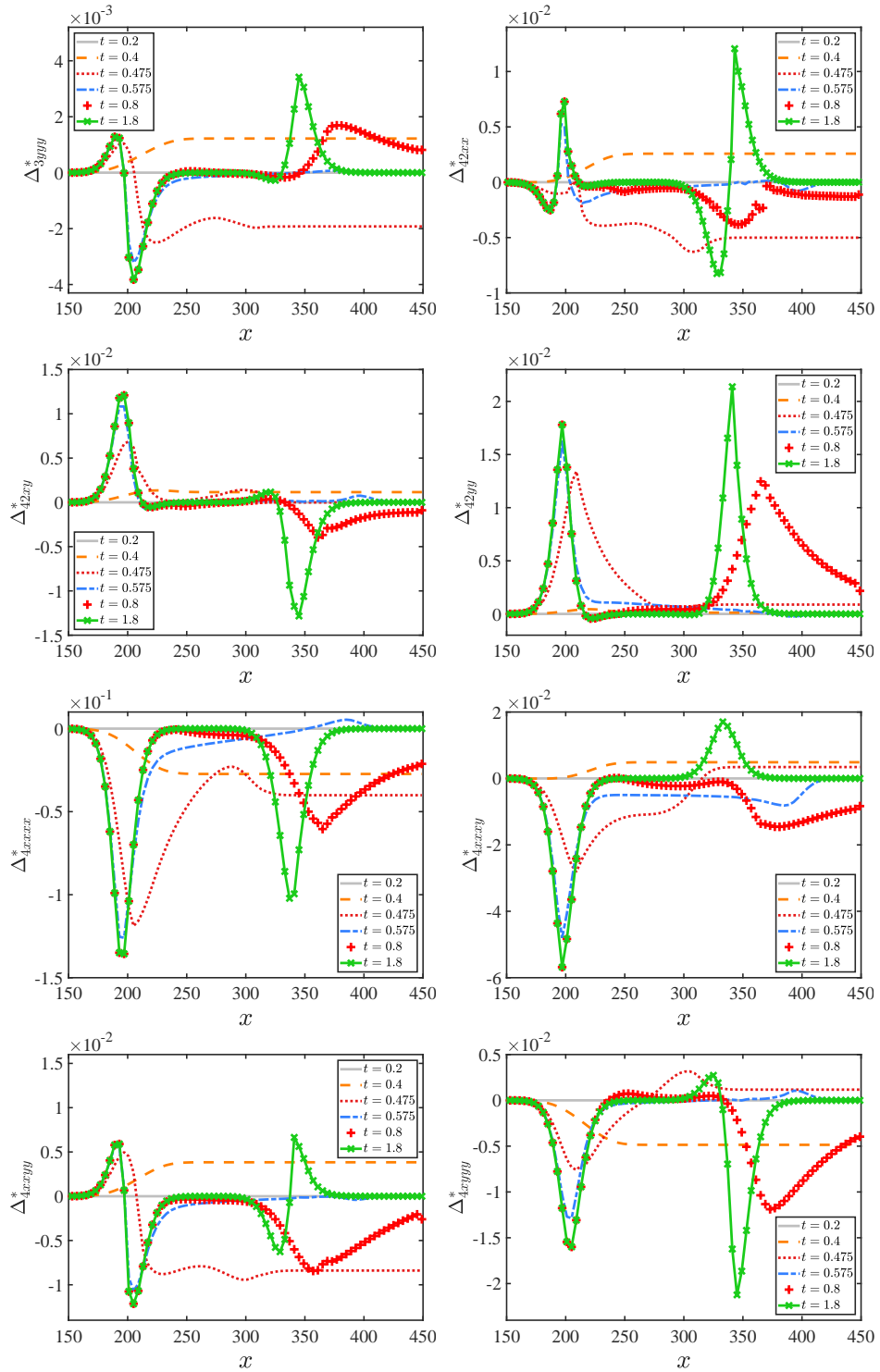
It should be noted that the total nonequilibrium strength shown in figures 13 and 14 is presented in a highly condensed form to represent the nonequilibrium state. The TNE characteristic quantities  $\Delta_2^*$ ,  $\Delta_{3,1}^*$ ,  $\Delta_3^*$ ,  $\Delta_{4,2}^*$ ,  $\Delta_4^*$ , and  $\Delta_{5,3}^*$  reflect the system's deviation from equilibrium from their respective perspectives, as illustrated in figure 17. These measures provide detailed nonequilibrium information at various temporal and spatial scales embedded in the flow field, which can be used to identify shock wave types, track their positions, and characterize their features.

From figure 17, the following common features can be observed:

(I) All nonequilibrium quantities,  $\Delta_2^*$ ,  $\Delta_{3,1}^*$ ,  $\Delta_3^*$ ,  $\Delta_{4,2}^*$ ,  $\Delta_4^*$ , and  $\Delta_{5,3}^*$ , exhibit peak values near the shock wave interface and decay to zero away from it. This is due to the large gradients in macroscopic quantities and strong nonequilibrium driving forces near the shock interface, causing a significant deviation from equilibrium.



(a) Continue.



(a) Continue.

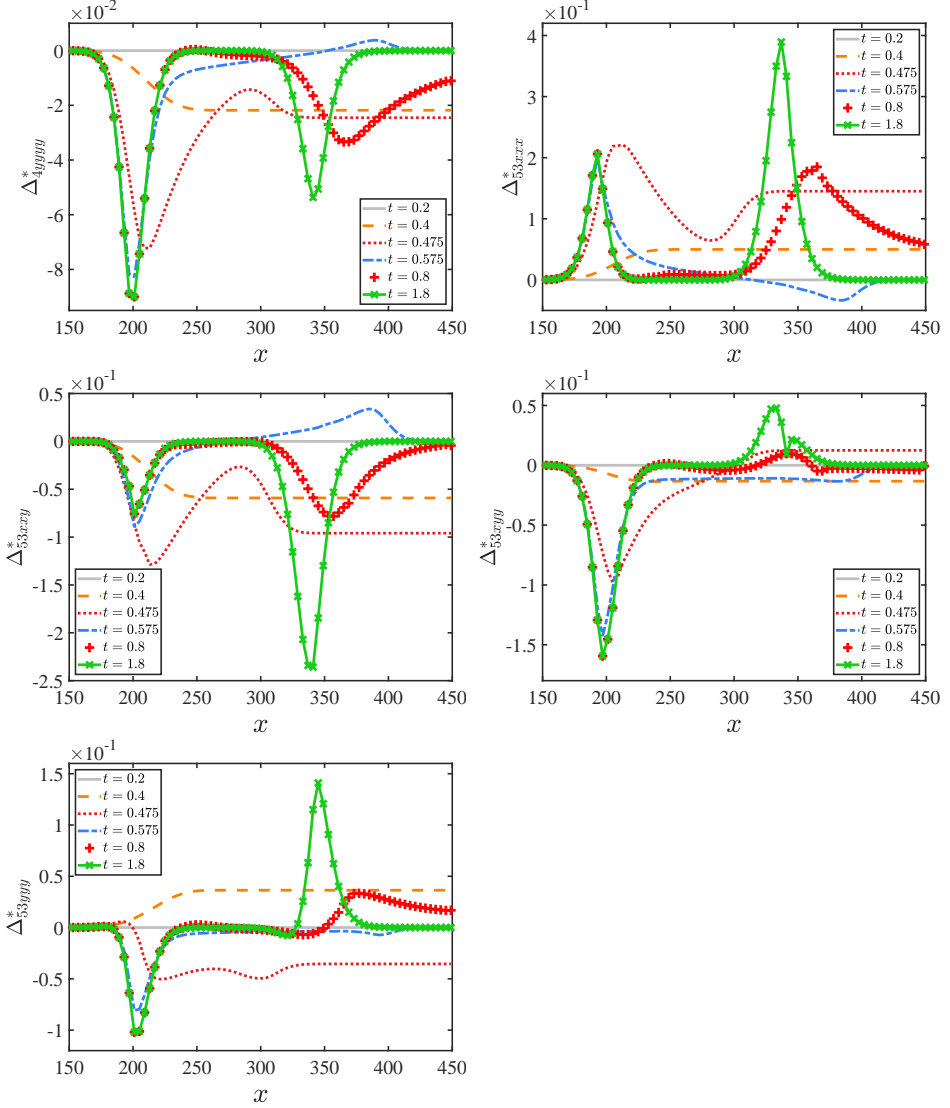


Figure 17: Distributions of typical nonequilibrium quantities  $\Delta_2^*$ ,  $\Delta_{3,1}^*$ ,  $\Delta_3^*$ ,  $\Delta_{4,2}^*$ ,  $\Delta_4^*$ , and  $\Delta_{5,3}^*$  along the line  $y = 40\Delta y$  at various instants.

(II) At the location of the incident shock wave, the peak positions of the nonequilibrium quantities shift downward over time. After the shock reaches the lower wall ( $t > 0.575$ ), under the influence of the solid wall, the peak positions of both the incident and reflected shock waves continue to shift leftward, while their amplitudes increase (except for  $\Delta_{2xx}^*$ ).

(III) At lower Mach numbers ( $Ma = 2.2$ ), the number of nonequilibrium effects dominant at the incident shock is approximately equal to those at the reflected shock. The relative dominance of different types of nonequilibrium effects within the same physical

process varies, reflecting the complexity of the system and highlighting the need for multi-perspective studies to fully understand its behavior.

(IV) For each nonequilibrium component, the first peak's appearance on the left (right) side corresponds to the time when the incident (reflected) shock wave moves downward (upward) to the current horizontal line. By observing the timing and position of the first peak at various heights, the formation of the incident and reflected shock waves can be tracked.

(V) Compared to  $t = 1.8$ , the deviation from equilibrium region is broader but weaker for  $t < 0.8$ , suggesting a wider but less intense curved reflected shock wave interface. However, at  $t = 0.8$ , most nonequilibrium components at the curved reflected shock wave location exhibit a significant amplitude increase, as the curved shock wave crosses the horizontal line  $y = 40\Delta y$ . This characteristic can be used to track the position of the curved shock wave and identify its transition to a straight shock wave. For example, at  $t = 0.8$ , the position  $x = 300$  corresponds to  $\Delta_{2xx}^*$ , aligning with the intersection of the curved shock wave and the line  $y = 40\Delta y$ , where all nonequilibrium quantities display this feature.

(VI) At  $t = 0.575$  and  $t = 0.8$ , the peak positions and amplitudes of the nonequilibrium components at the incident shock wave location are nearly identical. This provides strong evidence that the incident shock wave is about to compress and straighten, signaling its transition from a curved to an oblique shock wave. Similarly, at  $t = 1.3$  and  $t = 1.8$ , the peak positions and amplitudes of the nonequilibrium components at the reflected shock wave are also very close, providing clear evidence that the reflected shock wave is about to compress and straighten, signaling the transition from a curved to an oblique shock wave.

In addition to the common features outlined above, the differences among various nonequilibrium components are discussed as follows:

(I) The driving mechanisms of different nonequilibrium components are distinct, each describing the system's deviation from equilibrium from a unique perspective. These components are independent, non-interchangeable, and complementary, collectively providing an intuitive representation of the system's complex behavior.

(II) As time evolves, the peak value of  $\Delta_{2xx}^*$  at the location of the incident shock wave first decreases negatively, then increases positively. The shock interface initially widens and then gradually narrows, becoming progressively compressed.

(III) For  $t > 0.575$ , as the incident shock wave moves downward, the nonequilibrium interface, observed from the  $\Delta_{2xy}^*$  perspective, gradually broadens under the influence of the curved shock wave. Furthermore, the shear viscosity effect intensifies, causing the



shock wave to further curve and dissipate as it moves downward, resulting in a more extensive deviating-from-equilibrium region.

(IV) As the incident shock wave moves downward and reflects off the lower wall, energy is gradually transferred to the reflected shock wave, significant increasing  $\Delta_{2xy}^*$  and  $\Delta_{2yy}^*$  at the reflected shock wave. Before the peak at the reflected shock wave (at  $t = 1.8$ ), the curves of  $\Delta_{2xx}^*$  and  $\Delta_{2yy}^*$  exhibit symmetry.

(V) At  $t = 1.8$ ,  $\Delta_{3,1x}^*$  reaches its maximum at the reflected shock wave, indicating an intense interaction between the incident and reflected shock waves, with significant heat exchange. In addition, at this moment, the heat flux in the  $y$ -direction,  $\Delta_{3,1y}^*$ , shows a positive peak at the reflected shock wave, exceeding  $\Delta_{3,1x}^*$ , indicating greater heat transfer in the  $y$ -direction. This difference in peak values reveals the anisotropy of heat transfer during the interaction between the incident and reflected shock waves.

(VI) When  $t > 0.575$ , the viscous stress fluxes  $\Delta_{3xxy}^*$ ,  $\Delta_{3xyy}^*$ , and  $\Delta_{3yyy}^*$  gradually reach their peak values at the curved incident/reflected shock waves. As the shock waves straighten, their peak values increase further, indicating a stronger molecular motion within the shock. When  $0.475 \leq t \leq 0.8$ ,  $\Delta_{3xxx}^*$  reaches an equilibrium at the center of the shock wave, then deviates oppositely to reach a peak before returning to equilibrium further from the shock interface. These observations highlight the directional differences in the viscous stress flux  $\Delta_3^*$ , reflecting the anisotropic nature of the fluid's viscous response in different directions.

(VII) At  $t = 0.575$ , the flux of heat flux  $\Delta_{4,2xy}^*$  reaches its peak at the center of the curved incident shock. In contrast,  $\Delta_{4,2xx}^*$  and  $\Delta_{4,2yy}^*$  reach equilibrium at the center of the curved incident shock, with peaks on either side. When  $t \geq 0.8$ , at the center of the reflected shock, the peaks of  $\Delta_{4,2xx}^*$  and  $\Delta_{4,2xy}^*$  shift leftward over time, with their intensities gradually increasing. These findings provide key instantaneous characteristics for understanding the thermodynamic flux dynamics during regular shock wave reflection.

(VIII) For  $t \geq 0.475$ , peaks of  $\Delta_{4xxx}^*$ ,  $\Delta_{4xxy}^*$ ,  $\Delta_{4xyy}^*$ ,  $\Delta_{4yyy}^*$ , and  $\Delta_{4yyyy}^*$  are observed at the curved incident shock location. Additionally,  $\Delta_{4xxx}^*$ ,  $\Delta_{4xxy}^*$ , and  $\Delta_{4yyyy}^*$  reach positive peaks, while the remaining components exhibit negative values. Between  $0.475 \leq t \leq 0.575$ , these peaks shift leftward within the curved reflected shock region. These findings highlight temporal evolution characteristics of the anisotropic components of the viscous stress flux  $\Delta_4^*$  at the location of the curved incident shock. For  $t > 0.5$  the peaks of  $\Delta_{4xxx}^*$ ,  $\Delta_{4xxy}^*$ ,  $\Delta_{4xyy}^*$ , and  $\Delta_{4yyy}^*$  at the center of the curved reflected shock gradually increase over time, indicating intensified heat flux in specific directions during shock reflection.

(IX) For  $t \geq 0.475$ , peaks of  $\Delta_{5,3xxx}^*$ ,  $\Delta_{5,3xxy}^*$ ,  $\Delta_{5,3xyy}^*$ , and  $\Delta_{5,3yyy}^*$  are observed at the curved incident shock location. These peaks are particularly significant across all

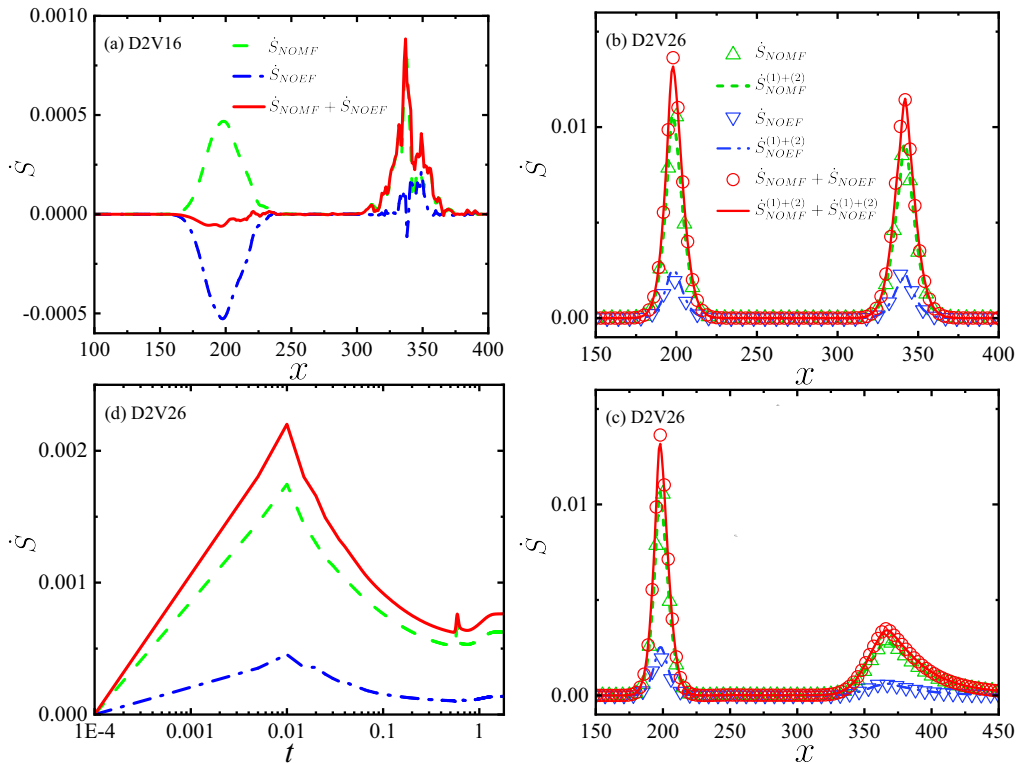


Figure 18: Entropy production rates obtained from the first-order DBM (a) and second-order DBM along the line  $y = 40\Delta y$  at  $t = 1.8$ , where the lines in (b) corresponding to theoretical solutions. (c) Entropy production rates along the same line at  $t = 0.8$ . (d) Evolution of entropy production rates during the regular shock wave reflection.

observation times. Notably, the peak value of  $\Delta_{5,3xxx}^*$  is positive, while the peak values of  $\Delta_{5,3xxy}^*$ ,  $\Delta_{5,3xyy}^*$ , and  $\Delta_{5,3yyy}^*$  are negative. This phenomenon also reveals the anisotropic spatial characteristics of the heat flux components. For  $t > 0.8$ , the peaks of  $\Delta_{5,3xxx}^*$ ,  $\Delta_{5,3xxy}^*$ ,  $\Delta_{5,3xyy}^*$ , and  $\Delta_{5,3yyy}^*$  at the curved reflected shock location gradually increase. This indicates that, as time progresses, the nonequilibrium heat flux dynamics in the curved reflected shock region continue to intensify, reflecting the complex evolution of the fluid structure during shock interaction.

#### 4.4. Entropy production mechanism

Figure 18(c) shows the entropy production rates from viscous stress, heat flux, and their sum along the line  $y = 40\Delta y$  at  $t = 0.8$ . The symbols represent DBM simulation results, while the lines show the corresponding second-order analytical solutions. Comparing with figure 17, it is clear that the entropy production rate is highly correlated with the nonequilibrium effects.

The entropy production rate peaks at  $x = 198$  and  $342$ , where both viscous stress and heat flux reach their maxima, exactly corresponding to the positions of incident and curved reflected shock waves. Therefore, by observing the peak positions and shapes of the entropy production rate curve, the evolution speed and morphological distribution of the shock waves can be dynamically characterized from a more fine view. In comparison with figure 18(c) at  $t = 1.8$ , the nonzero region of entropy production at the reflected shock wave is wider but less intense, due to the broad, uncompressed curved shock wave interface. As the reflected shock wave interacts with the wall, the curved shock wave is compressed and straightened, increasing the intensity of entropy production and shifting the peak position leftward. Throughout the regular shock wave reflection process, the contribution of heat flux to entropy production is much smaller than that of viscous stress, especially at the curved shock wave, indicating that the process is predominantly by viscous stress.

Figure 18(d) illustrates the evolution of the three types of entropy production over time. The entropy production rate initially increases, then decreases, increases again, and finally stabilizes. At  $t = 0.01$ , the entropy production rate rapidly reaches its maximum due to the nonequilibrium driving force caused by the initial macroscopic gradient. At this point, the system has not yet undergone dissipation. The shock interface is narrow, and the entropy production rate due to stress reaches its peak earlier than that due to heat flux. This suggests that viscous stress, driven by sustained incoming flow from the left and upper boundaries, is the dominant driving force of the system. At  $t = 0.59$ , a local peak in entropy production arises due to the formation of the curved incident shock wave, which enlarges the nonequilibrium region. Afterward, as the incident shock wave interacts with the lower wall and the curved reflected shock wave forms, entropy production slowly increases, until  $t = 1.35$ , when it stabilizes.

Figure 19 shows the temporal evolution of dimensionless nonequilibrium intensities. The intensities of various nonequilibrium quantities span several orders of magnitude. Starting from an initial nonequilibrium state,  $|\Delta_{m,n}^*|$  first shows a sharp increase, followed by a gradual approach toward thermodynamic equilibrium. This behavior results from the strong correlation between TNE effects and interface dynamics, which are characterized by varying area and morphological complexity.

Higher-order TNE dynamic modes play a more significant role compared to their lower-order counterparts, and dominate the total nonequilibrium intensity. Additionally, the relative strength of dynamic modes varies across different stages. For example,  $|\Delta 2^*|$  is initially weaker than  $|\Delta 3, 1^*|$ , but this relationship reverses at later stages. Overall, their evolution trends closely align with that of entropy production rates. At  $t = 0.6$ , a slight jump in  $|\Delta 3, 1^*|$  and  $|\Delta 4, 2^*|$  marks the moment when the incident shock wave reaches

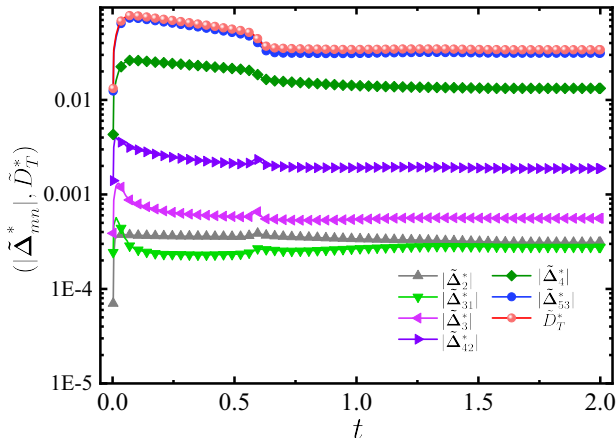


Figure 19: Evolution of dimensionless nonequilibrium intensities from various perspectives.

the bottom wall. This change serves as an indicator for determining the time of shock wave reflection.

In fact, the entropy production rate and TNE intensity, analyzed from different perspectives, provide a comprehensive view of the system's nonequilibrium characteristics. These detailed dynamics complement the synthetic TNE strength  $\tilde{D}_T^*$  and macroscopic conserved quantities typically considered in traditional fluid mechanics.

#### 4.5. Effects of Mach number on thermodynamic nonequilibrium effects

In practical engineering applications, the range of Mach numbers involved is quite broad. A higher Mach number corresponds to a greater compression effect and higher pressure ratio, density ratio, and temperature jump, resulting in stronger interaction between the shock wave and the medium. To explore the influence of Mach number on nonequilibrium intensity during oblique shock wave reflection, simulations were performed for Mach numbers ranging from 2.1 to 5.1, with increments of 0.3 and an incident angle of  $29^\circ$ .

Figure 20 illustrates the effects of Mach number on the peak values of various nonequilibrium measures at  $t = 0.8$  and  $y = 10\Delta y$ . The left column shows results for the incident shock, and the right column corresponds to the reflected shock. The circles and solid lines in each panel represent the DBM simulation results and the nonlinear fitting results, respectively. From figure 20, it is evident that:

(I) The nonequilibrium intensity increases significantly with the order  $m$  of the nonequilibrium quantities.

(II) The Mach number  $Ma$  exponentially amplifies the nonequilibrium intensity  $\tilde{D}_{m,n}^*$ .

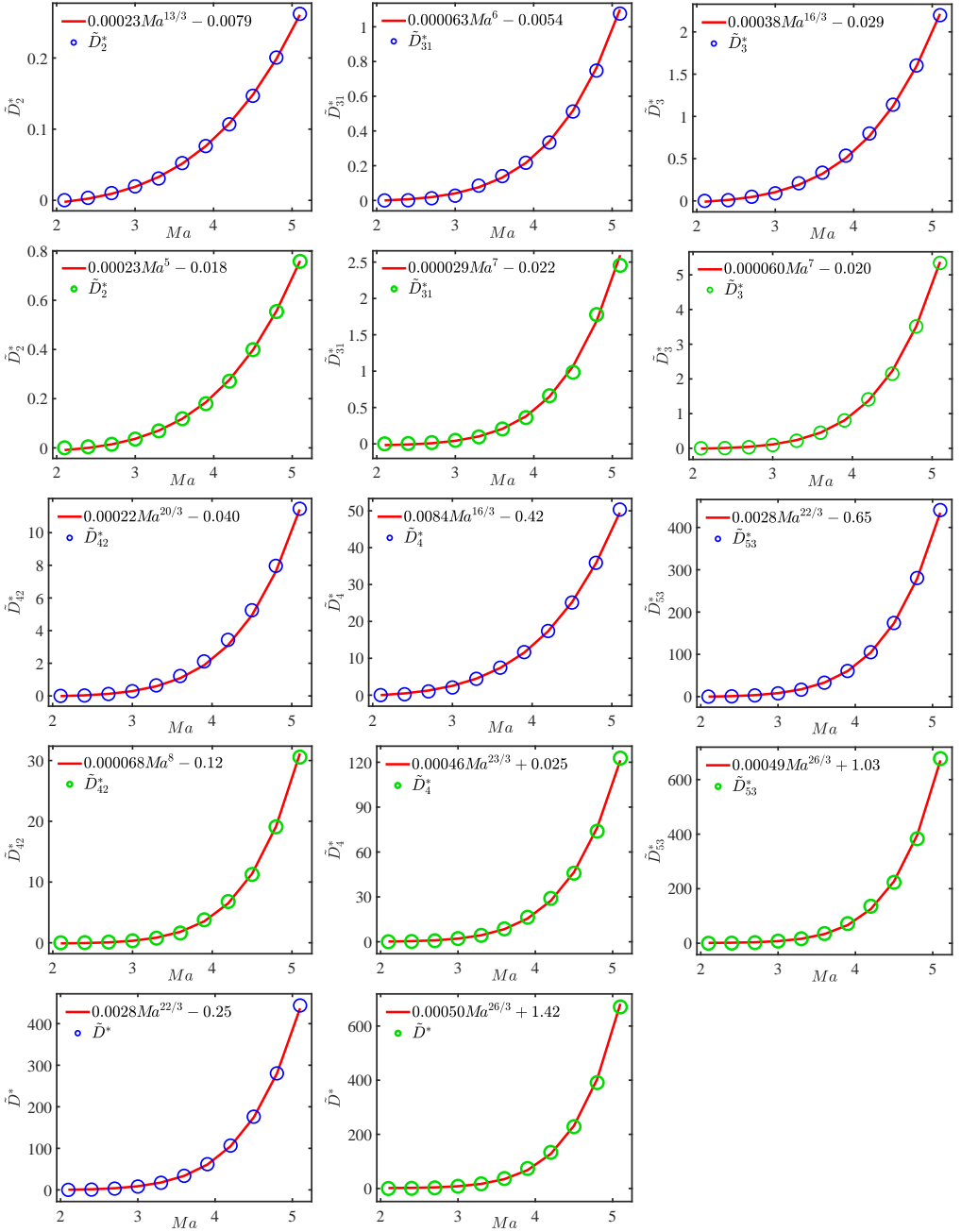


Figure 20: Effects of Mach number on the peak values of various nonequilibrium measures. The blue circles represent the DBM simulation results at the incident shock, while the green circles correspond to those at the reflected shock. The red solid lines show the nonlinear fits to the simulation data.

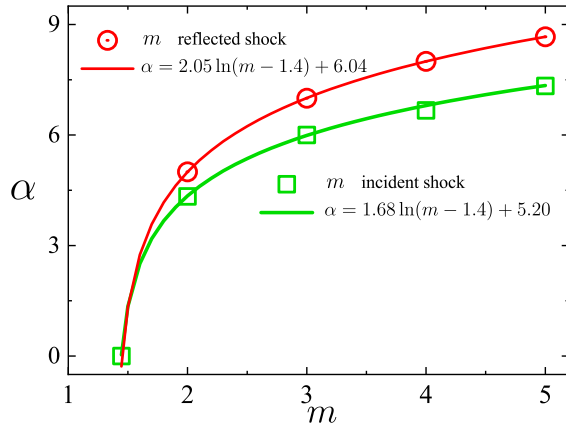


Figure 21: The correlations between the Mach number growth exponent  $\alpha$  and the order of nonequilibrium quantities  $m$  at both the incident and reflected shocks.

(III) The growth exponent of the Mach number  $\alpha$  for higher-order nonequilibrium quantities is substantially larger than that for lower-order quantities. For instance:

- $\tilde{D}_2 \sim Ma^{13/3}$  (left column)  $\sim Ma^5$  (right column),
- $\tilde{D}_{5,3} \sim Ma^{22/3}$  (left column)  $\sim Ma^{26/3}$  (right column).

This suggests that higher-order quantities are more sensitive to variations in the Mach number.

(IV) The peak values of nonequilibrium intensity at the reflected shock are consistently higher than those at the incident shock. This difference arises from the interaction between the reflected shock and the wall, which generates stronger local nonequilibrium effects. Additionally, this highlights the greater sensitivity of the nonequilibrium intensity at the reflected shock to variations in the Mach number.

(V) The intercept (constant term) of the fitted curves is nearly zero for the incident shock but much larger for the reflected shock. This behavior is attributed to the more complex structure and stronger local macroscopic gradients at the reflected shock.

To further clarify the trends discussed above, figure 21 presents the correlations between the Mach number growth exponent  $\alpha$  and the order of nonequilibrium quantities  $m$  for both the incident and reflected shocks. Key observations include: (1) For both incident and reflected shocks, the growth exponent  $\alpha$  increases logarithmically with the order  $m$  of the nonequilibrium quantities:  $\alpha \sim \ln(m - c)$ , where  $c$  is a constant. This indicates that higher-order nonequilibrium quantities are more sensitive to variations in the Mach number. As  $m$  increases, the growth rate of  $\alpha$  slows but still shows a progressive enhancement. (2) The curve for the reflected shock consistently lies above the curve for the incident shock and has a larger intercept. For the same order of nonequilibrium quantity  $m$ , the growth exponent  $\alpha$  is considerably higher at the reflected shock than at

the incident shock. This underscores the stronger nonequilibrium effects at the reflected shock.

## 5. Discussion, conclusions, and recommendations

The challenges in simulating supersonic flow can be categorized into two types: one arises from the equation solvers, such as discrete schemes, and the other from the physical model itself. The limitations of the physical model cannot be overcome by enhancing algorithmic accuracy and efficiency. Early studies predominantly relied on the Navier-Stokes (NS) equations, which are based on the quasi-continuum assumption and the near-equilibrium approximation. However, mesoscale structures, such as shock waves, are small-scale structures, and compared to the shock thickness, the mean molecular spacing is no longer a negligible small quantity, leading to increased discreteness. The physical quantities across the shock change abruptly, signifying a rapid process. As these quantities vary, the system lacks sufficient time to return to thermodynamic equilibrium, resulting in a higher degree of nonequilibrium. The quasi-continuum model fails to capture discrete effects, such as rarefaction, while the near-equilibrium model is inadequate for describing strong non-equilibrium behaviors. Furthermore, the lack of advanced techniques for analyzing complex physical fields results in significant data resource waste. As discretization and rarefaction increase, the description of the system state demands more state variables, and the characterization of effects necessitates additional variables. This is an inevitable requirement to accurately describe physical mechanisms as discretization and rarefaction increase. The primary technical challenge is determining which physical variables need to be added. A typical feature of supersonic flow is that even a small change can trigger widespread effects. Previous insights, based on slow variables, conserved quantities, and the Knudsen number defined from a single perspective, have been incomplete or inaccurate.

In response to these issues, this paper develops a more effective approach for constructing physical models and a more refined technique for analyzing complex physical fields—the discrete Boltzmann method (DBM), to study the multiscale, nonequilibrium, and complex behavior of supersonic flows. The key conclusions are summarized as follows: (1) A Burnett-level DBM model, tailored for supersonic flows, is developed based on the Shakhov-BGK framework. It provides higher-order analytical expressions for typical thermodynamic nonequilibrium effects, forming a constitutive foundation for improving traditional macroscopic hydrodynamic models. (2) Criteria for validating the DBM model are established by comparing numerical solutions with analytical results for nonequilibrium effects. (3) The multiscale DBM is applied to analyze nonequilibrium characteristics

and entropy production mechanisms in shock wave reflections. Compared to Navier-Stokes-level DBM, the Burnett-level DBM offers: (a) More accurate representations of viscous stress and heat flux, i.e., dissipative mechanisms; (b) Consistency with the second law of thermodynamics by ensuring non-negative entropy production; (c) Improved numerical stability. (d) Near the interfaces of incident and reflected shock waves, strong nonequilibrium driving forces result in prominent nonequilibrium effects. The distribution and evolution of these effects in shock reflections suggest that nonequilibrium quantities are critical indicators for tracking complex flow processes. This is particularly valuable for understanding shock interface dynamics. (e) In intermediate states of shock reflections, the bent reflected shock and incident shock interfaces are wider and exhibit lower nonequilibrium intensities than in the final state. This observation can be used to track the position and straightening process of the bent shock. (f) The Mach number enhances nonequilibrium intensities in a power-law manner. The power-law exponent and the order of nonequilibrium dynamic modes follow a logarithmic relationship. This study provides kinetic insights into the modeling and analysis of supersonic flows, providing additional perspectives for further exploration of nonequilibrium and multiscale phenomena in complex flow systems.

Future research should focus on the following directions: (1) Model extensions: Further expand DBM models to accommodate more complex physical scenarios, such as chemically reactive or multiphase supersonic flows. (2) Nonequilibrium diagnostics and regulations: Develop diagnostic and control techniques based on nonequilibrium quantities and corresponding analytical solutions for achieving engineering optimization of complex flow processes.

## **Acknowledgements**

We acknowledge support from the National Natural Science Foundation of China (Grant Nos. 11875001 and 12172061), Hebei Outstanding Youth Science Foundation (Grant No. A2023409003), the Central Guidance on Local Science and Technology Development Fund of Hebei Province (Grant No. 226Z7601G), Foundation of National Key Laboratory of Shock Wave and Detonation Physics (Grant No. JCKYS2023212003), and the opening project of State Key Laboratory of Explosion Science and Technology (Beijing Institute of Technology) (Grant No. KFJJ23-02M), the Foundation of the National Key Laboratory of Computational Physics (Grant No. SYSQN2024-10), the High-level Talents Research Start-up Grant from Guangxi University (Grant No. ZX01080031224009).



## Declaration of interests

The authors report no conflict of interest.

## Appendix A. Second-order analytical expressions for viscous stress and heat flux

The contributions of the second-order deviation of the distribution function  $f^{(2)}$  to viscous stress and heat flux are detailed as follows::

$$\Delta_{2xx}^{*(2)} = 2n_2^{-1}\tau^2 \left\{ \begin{array}{l} n_2^{-1}\rho RT \left[ n_{-2}n_1(\partial_x u_x)^2 + n_1n_2(\partial_y u_x)^2 \right. \\ \left. - 4n\partial_x u_x \partial_y u_y - n_2(\partial_x u_y)^2 - n_{-2}(\partial_y u_y)^2 \right] \\ - R^2 T^2 (n_1 \frac{\partial^2 \rho}{\partial x^2} - \frac{\partial^2 \rho}{\partial y^2}) \\ + \frac{R^2 T^2}{\rho} \left[ n_1(\partial_x \rho)^2 - (\partial_y \rho)^2 \right] + \frac{\rho R^2}{Pr} \left[ n_1(\partial_x T)^2 - (\partial_y T)^2 \right] \\ + \rho R^2 T (\frac{1}{Pr} - 1) (n_1 \frac{\partial^2 T}{\partial x^2} - \frac{\partial^2 T}{\partial y^2}) + R^2 T (\frac{1}{Pr} - 1) (n_1 \partial_x \rho \partial_x T - \partial_y \rho \partial_y T) \end{array} \right\} \quad (A 1)$$

$$\Delta_{2xy}^{*(2)} = 2\tau^2 \left\{ \begin{array}{l} \rho RT n_2^{-1} (-2\partial_x u_x \partial_y u_x + n\partial_x u_x \partial_x u_y + n\partial_y u_x \partial_y u_y - 2\partial_x u_y \partial_y u_y) \\ - R^2 T^2 \frac{\partial^2 \rho}{\partial x \partial y} + \frac{R^2 T^2}{\rho} \partial_x \rho \partial_y \rho + \frac{\rho R^2}{Pr} \partial_x T \partial_y T + \rho R^2 T (\frac{1}{Pr} - 1) \frac{\partial^2 T}{\partial x \partial y} \\ + \frac{R^2 T}{2} (\frac{1}{Pr} - 1) (\partial_x \rho \partial_y T + \partial_y \rho \partial_x T) \end{array} \right\} \quad (A 2)$$

$$\Delta_{2yy}^{*(2)} = 2n_2^{-1}\tau^2 \left\{ \begin{array}{l} n_2^{-1}\rho RT \left[ n_{-2}n_1(\partial_y u_y)^2 + n_1n_2(\partial_x u_y)^2 \right. \\ \left. - 4n\partial_x u_x \partial_y u_y - n_2(\partial_y u_x)^2 - n_{-2}(\partial_x u_x)^2 \right] \\ - R^2 T^2 (n_1 \frac{\partial^2 \rho}{\partial y^2} - \frac{\partial^2 \rho}{\partial x^2}) + \frac{R^2 T^2}{\rho} \left[ n_1(\partial_y \rho)^2 - (\partial_x \rho)^2 \right] \\ + \frac{\rho R^2}{Pr} \left[ n_1(\partial_y T)^2 - (\partial_x T)^2 \right] + \rho R^2 T (\frac{1}{Pr} - 1) (n_1 \frac{\partial^2 T}{\partial y^2} - \frac{\partial^2 T}{\partial x^2}) \\ + R^2 T (\frac{1}{Pr} - 1) (n_1 \partial_y \rho \partial_y T - \partial_x \rho \partial_x T) \end{array} \right\} \quad (A 3)$$

$$\Delta_{3,1x}^{*(2)} = n_2^{-1} \frac{\tau^2 \rho R^2 T}{Pr^2} \left\{ \begin{array}{l} T[(2n_1 Pr - n_4) \frac{\partial^2 u_x}{\partial x^2} + (n Pr - n_4) \frac{\partial^2 u_y}{\partial x \partial y} + n_2 Pr \frac{\partial^2 u_x}{\partial y^2}] \\ + (n_1 n_6 Pr + n_{-2}) \partial_x u_x \partial_x T + \frac{n_2 n_6 (Pr + 1)}{2} \partial_y u_x \partial_y T \\ - n_6 (Pr + 1) \partial_y u_y \partial_x T + (\frac{n_2 n_6 Pr - n_{-2}^2}{2}) \partial_x u_y \partial_y T \end{array} \right\} \quad (A 4)$$

$$\Delta_{3,1y}^{*(2)} = n_2^{-1} \frac{\tau^2 \rho R^2 T}{Pr^2} \left\{ \begin{array}{l} T[(2n_1 Pr - n_4) \frac{\partial^2 u_y}{\partial y^2} + (n Pr - n_4) \frac{\partial^2 u_x}{\partial x \partial y} + n_2 Pr \frac{\partial^2 u_y}{\partial x^2}] \\ + (n_1 n_6 Pr + n_{-2}) \partial_y u_y \partial_y T + \frac{n_2 n_6 (Pr + 1)}{2} \partial_x u_y \partial_x T \\ - n_6 (Pr + 1) \partial_x u_x \partial_y T + (\frac{n_2 n_6 Pr - n_{-2}^2}{2}) \partial_y u_x \partial_x T \end{array} \right\} \quad (A 5)$$

Here  $n_a = n + a$ , for example  $n_1 = n + 1$ .

The second-order analytical expressions indicate that viscous stress depends not only on velocity gradients but also on additional terms, including:

(1) Squared velocity gradient terms, such as  $(\partial_\alpha u_\alpha)^2$  and  $(\partial_\alpha u_\beta)^2$ , capture the nonlinear effects of velocity variations. These terms represent the intensity of local variations rather than just the direction or rate of change. Such intense variations can lead to local

stress concentrations. For example,  $(\partial_\alpha u_\alpha)^2$  may cause local compression or rarefaction, while  $(\partial_\alpha u_\beta)^2$  can induce local shear.

(2) The squared term of density gradients,  $(\partial_\alpha \rho)^2$ , reflects the intensity of density variations and affects local compressive stress and flow stability

(3) The second-order derivatives of density,  $\frac{\partial^2 \rho}{\partial \alpha^2}$ , represent the curvature of density in  $\alpha$  direction. This curvature reflects the degree of bending in the density distribution and the compressive behavior of the fluid in specific regions. Such changes in curvature can lead to local volume responses and variations in stress within the fluid. Both terms (2) and (3) highlight the impact of density inhomogeneity on viscous stress, mediated by the compressibility of the fluid.

(4) The squared temperature gradient term,  $(\partial_\alpha T)^2$ , reflects the intensity of temperature gradients and mainly affects thermal convection. This, in turn, influences viscous stress by altering both the strength and mode of convection.

(5) The second-order derivatives of temperature,  $\frac{\partial^2 T}{\partial \alpha^2}$ , reflect the curvature of temperature and primarily affect the rate of thermal diffusion. Consequently, they influence viscous stress by affecting heat diffusion within the fluid.

(6) Coupled viscous stress terms, such as  $\partial_\alpha \rho \partial_\alpha T$ , represent the interaction between density and temperature gradients.

The term  $\Delta_{2xy}^{*(2)}$  includes additional coupling and cross-derivative terms. The term  $\Delta_{2yy}^{*(2)}$  contains the same additional terms as  $\Delta_{2xx}^{*(2)}$ .

Heat flux depends not only on temperature gradients but also on additional terms, including:

(1) The second-order derivatives of velocity,  $\frac{\partial^2 u_\alpha}{\partial \beta^2}$ , reflect contribution of fluid diffusion to heat flux.

(2) Coupled heat flux terms, such as  $\partial_\beta u_\beta \partial_\alpha T$ ,  $\partial_\beta u_\alpha \partial_\beta T$ , and  $\partial_\alpha u_\beta \partial_\beta T$ , reflect how velocity gradients regulate thermal flux.

## Appendix B. Independent kinetic moments required to fully characterize first- and second-order viscous stress and heat flux

To fully characterize first- and second-order viscous stress and heat flux, the Shakhov distribution function  $f^S$  needs to satisfy the following kinetic moments:

$$M_0^S = \rho \tag{B1}$$

$$M_{1x}^S = \rho u_x \tag{B2}$$

$$M_{1y}^S = \rho u_y$$

$$M_{2,0}^S = \frac{\rho}{2}(u_x^2 + u_y^2 + n_2 RT) \tag{B3}$$

$$\begin{aligned}
M_{2xx}^S &= \rho(u_x^2 + RT) \\
M_{2xy}^S &= \rho u_x u_y \\
M_{2yy}^S &= \rho(u_y^2 + RT)
\end{aligned} \tag{B4}$$

$$\begin{aligned}
M_{3,1x}^S &= \frac{\rho u_x}{2}(u_x^2 + u_y^2 + n_4 RT) + (1 - \text{Pr})q_x \\
M_{3,1y}^S &= \frac{\rho u_y}{2}(u_x^2 + u_y^2 + n_4 RT) + (1 - \text{Pr})q_y
\end{aligned} \tag{B5}$$

$$\begin{aligned}
M_{3xxx}^S &= \rho u_x(u_x^2 + 3RT) + 6n_4^{-1}(1 - \text{Pr})q_x \\
M_{3xxy}^S &= \rho u_y(u_x^2 + RT) + 2n_4^{-1}(1 - \text{Pr})q_y \\
M_{3xyy}^S &= \rho u_x(u_y^2 + RT) + 2n_4^{-1}(1 - \text{Pr})q_x \\
M_{3yyy}^S &= \rho u_y(u_y^2 + 3RT) + 6n_4^{-1}(1 - \text{Pr})q_y
\end{aligned} \tag{B6}$$

$$\begin{aligned}
M_{4,2xx}^S &= \frac{\rho}{2} [u_x^2(u_x^2 + u_y^2) + n_4 R^2 T^2 + (n_7 u_x^2 + u_y^2)RT] \\
&\quad + 2n_4^{-1}(1 - \text{Pr})(n_7 u_x q_x + u_y q_y) \\
M_{4,2xy}^S &= \frac{\rho}{2} [u_x u_y(u_x^2 + u_y^2) + n_6 u_x u_y RT] \\
&\quad + n_6 n_4^{-1}(1 - \text{Pr})(u_x q_y + u_y q_x) \\
M_{4,2yy}^S &= \frac{\rho}{2} [u_y^2(u_x^2 + u_y^2) + n_4 R^2 T^2 + (n_7 u_y^2 + u_x^2)RT] \\
&\quad + 2n_4^{-1}(1 - \text{Pr})(n_7 u_y q_y + u_x q_x)
\end{aligned} \tag{B7}$$

$$\begin{aligned}
M_{4xxxx}^S &= \rho [u_x^2(u_x^2 + 6RT) + 3R^2 T^2] + 24n_4^{-1}(1 - \text{Pr})u_x q_x \\
M_{4xxyy}^S &= \rho u_x u_y(u_x^2 + 3RT) + 6n_4^{-1}(1 - \text{Pr})(u_x q_y + u_y q_x) \\
M_{4xxyy}^S &= \rho [u_x^2 u_y^2 + (u_x^2 + u_y^2)RT + R^2 T^2] \\
&\quad + 4n_4^{-1}(1 - \text{Pr})(u_x q_x + u_y q_y) \\
M_{4xyyy}^S &= \rho u_x u_y(u_y^2 + 3RT) + 6n_4^{-1}(1 - \text{Pr})(u_x q_y + u_y q_x) \\
M_{4yyyy}^S &= \rho [u_y^2(u_y^2 + 6RT) + 3R^2 T^2] + 24n_4^{-1}(1 - \text{Pr})u_y q_y
\end{aligned} \tag{B8}$$

$$\begin{aligned}
M_{5,3xxx}^S &= \frac{\rho}{2} [u_x^3(u_x^2 + u_y^2) + 3n_6 u_x R^2 T^2 + (n_{11} u_x^2 + 3u_y^2)u_x RT] \\
&\quad + 3n_4^{-1}(1 - \text{Pr}) [q_x(n_{11} u_x^2 + u_y^2 + 2n_6 RT) + 2u_x u_y q_y] \\
M_{5,3xxy}^S &= \frac{\rho}{2} [u_x^2 u_y(u_x^2 + u_y^2) + n_6 u_y R^2 T^2 + (n_9 u_x^2 + u_y^2)u_y RT] \\
&\quad + n_4^{-1}(1 - \text{Pr}) [q_y(n_9 u_x^2 + 3u_y^2 + 2n_6 RT) + 2n_9 u_x u_y q_x] \\
M_{5,3xyy}^S &= \frac{\rho}{2} [u_x u_y^2(u_x^2 + u_y^2) + n_6 u_x R^2 T^2 + (n_9 u_y^2 + u_x^2)u_x RT] \\
&\quad + n_4^{-1}(1 - \text{Pr}) [q_x(n_9 u_y^2 + 3u_x^2 + 2n_6 RT) + 2n_9 u_x u_y q_y] \\
M_{5,3yyy}^S &= \frac{\rho}{2} [u_y^3(u_x^2 + u_y^2) + 3n_6 u_y R^2 T^2 + (n_{11} u_y^2 + 3u_x^2)u_y RT] \\
&\quad + 3n_4^{-1}(1 - \text{Pr}) [q_y(n_{11} u_y^2 + u_x^2 + 2n_6 RT) + 2u_x u_y q_x],
\end{aligned} \tag{B9}$$

$$\begin{aligned}
 & \text{Gan, Zhuang, Yang, Xu, Zhang, Chen, Song, Wu} \\
 M_{4,0}^S = & \frac{\rho}{2} \left[ (u_x^2 + u_y^2)^2 + n_2 n_4 R^2 T^2 + 2n_4 (u_x^2 + u_y^2) RT \right] \\
 & + 4(1 - \text{Pr})(u_x q_x + u_y q_y).
 \end{aligned}
 \tag{B 10}$$

When  $\text{Pr} = 1$ , the above equations condense into the moment relations that  $f^{ea}$  must satisfy to fully characterize first- and second-order viscous stress and heat flux.

## REFERENCES

- BAO, Y., QIU, R., ZHOU, K., ZHOU, T., WENG, Y., LIN, K. & YOU, Y. 2022 Study of shock wave/boundary layer interaction from the perspective of nonequilibrium effects. *Phys. Fluids* **34** (4).
- CAI, H., YAN, X., YAO, P. & ZHU, S. 2021 Hybrid fluid-particle modeling of shock-driven hydrodynamic instabilities in a plasma. *Matter Radiat. Extremes* **6** (3).
- CHANG, J., LI, N., XU, K., BAO, W. & YU, D. 2017 Recent research progress on unstart mechanism, detection and control of hypersonic inlet. *Prog. Aerosp. Sci.* **89**, 1–22.
- CHEN, F., XU, A., SONG, J., GAN, Y., ZHANG, Y. & GUAN, N. 2024a Surface tension effects on Rayleigh-Taylor instability in nonideal fluids: A multiple-relaxation-time discrete Boltzmann study. *Sci. China Phys. Mech. Astron* **67** (12), 124611.
- CHEN, J., XU, A., ZHANG, Y., CHEN, D. & CHEN, Z. 2024b Kinetics of Rayleigh-Taylor instability in van der Waals fluid: the influence of compressibility. *Front. Phys.* **20** (1), 011201.
- CHEN, J., ZHANG, Y. & GUO, Y. 2019 *Numerical Simulation Methods and Applications for Hypersonic Flows*. Science Press.
- DANEHY, P., BATHEL, B., JOHANSEN, C., WINTER, M., O'BYRNE, S. & CUTLER, A. 2015 Molecular-based optical diagnostics for hypersonic nonequilibrium flows. *Tech. Rep.* 12.
- EU, B. C. 1992 Kinetic theory and irreversible thermodynamics. *NASA STI/Recon Technical Report A* **93**, 24498.
- GAN, Y., XU, A., LAI, H., LI, W., SUN, G. & SUCCI, S. 2022 Discrete Boltzmann multi-scale modelling of non-equilibrium multiphase flows. *J. Fluid Mech.* **951**, A8.
- GAN, Y.B., XU, A.G., ZHANG, G.C., LIN, C.D., LAI, H.L. & LIU, Z.P. 2019 Nonequilibrium and morphological characterizations of Kelvin-Helmholtz instability in compressible flows. *Front. Phys.* **14**, 1–17.
- GAN, Y., XU, A., ZHANG, G. & SUCCI, S. 2015 Discrete Boltzmann modeling of multiphase flows: hydrodynamic and thermodynamic non-equilibrium effects. *Soft Matter* **11** (26), 5336–5345.
- GAN, Y., XU, A., ZHANG, G. & YANG, Y. 2013 Lattice BGK kinetic model for high speed compressible flows: hydrodynamic and nonequilibrium behaviors. *EPL* **103** (2), 24003.
- GAN, Y., XU, A., ZHANG, G., YU, X. & LI, Y. 2008 Two-dimensional lattice Boltzmann model for compressible flows with high Mach number. *Physica A* **387** (8–9), 1721–1732.
- GAN, Y., XU, A., ZHANG, G., ZHANG, Y. & SUCCI, S. 2018 Discrete Boltzmann trans-scale modeling of high-speed compressible flows. *Phys. Rev. E* **97** (5), 053312.
- GU, S. & OLIVIER, H. 2020 Capabilities and limitations of existing hypersonic facilities. *Prog. Aerosp. Sci.* **113**, 100607.

- GUO, Z. & SHU, C. 2013 *Lattice Boltzmann method and its application in engineering*, vol. 3. World Scientific.
- GUO, Z., WANG, R. & XU, K. 2015 Discrete unified gas kinetic scheme for all knudsen number flows. II. thermal compressible case. *Phys. Rev. E* **91** (3), 033313.
- HUANG, W. AND LI, J. & EDWARDS, P. P. 2018 Mesoscience: exploring the common principle at mesoscales. *Natl. Sci. Rev.* **5** (3), 321–326.
- HUANG, W., WU, H., YANG, Y., YAN, L. & LI, S. 2020 Recent advances in the shock wave/boundary layer interaction and its control in internal and external flows. *Acta Astronaut.* **174**, 103–122.
- JI, YU, LIN, C. & LUO, K. H. 2022 A three-dimensional discrete Boltzmann model for steady and unsteady detonation. *J. Comput. Phys.* **455**, 111002.
- JIANG, Z., HU, Z., WANG, Y. & HAN, G. 2020 Advances in critical technologies for hypersonic and high-enthalpy wind tunnel. *Chin. J. Aeronaut.* **33** (12), 3027–3038.
- JIANG, Z., ZHAO, W., YUAN, Z., CHEN, W. & MYONG, R.S. 2019 Computation of hypersonic flows over flying configurations using a nonlinear constitutive model. *AIAA J.* **57** (12), 5252–5268.
- KALLIKOUNIS, N. G., DORSCHNER, B. & KARLIN, I. V. 2022 Particles on demand for flows with strong discontinuities. *Phys. Rev. E* **106** (1), 015301.
- KHOTYANOVSKY, D. K., BONDAR, Y. A., KUDRYAVTSEV, A. N., SHOEV, G. V. & IVANOV, M. S. 2009 Viscous effects in steady reflection of strong shock waves. *AIAA J.* **47** (5), 1263–1269.
- LAI, H., XU, A., ZHANG, G., GAN, Y., YING, Y. & SUCCI, S. 2016 Nonequilibrium thermohydrodynamic effects on the Rayleigh-Taylor instability in compressible flows. *Phys. Rev. E* **94** (2), 023106.
- LAW, C. K. 2010 *Combustion physics*. Cambridge university press.
- LI, H. & BEN-DOR, G. 1997 A parametric study of mach reflection in steady flows. *J. Fluid Mech.* **341**, 101–125.
- LI, S. & XIAO, H. 2021 A unified theory for modelling nonequilibrium and equilibrium gas flows. *Acta Astronaut.* **182**, 486–497.
- LI, S. G., GAO, B. & WU, Z. N. 2011 Time history of regular to mach reflection transition in steady supersonic flow. *J. Fluid Mech.* **682**, 160–184.
- LI, Z. H., PENG, A. P., ZHANG, H. X. & YANG, J.Y. 2015 Rarefied gas flow simulations using high-order gas-kinetic unified algorithms for Boltzmann model equations. *Prog. Aerosp. Sci.* **74**, 81–113.
- LI, Z. H. & ZHANG, H. X. 2009 Gas-kinetic numerical studies of three-dimensional complex flows on spacecraft re-entry. *J. Comput. Phys.* **228** (4), 1116–1138.
- LIN, C., LUO, K. H. & FEI, L. AND SUCCI, S. 2017 A multi-component discrete Boltzmann model for nonequilibrium reactive flows. *Sci. Rep.* **7** (1), 14580.
- LIU, H., KANG, W., ZHANG, Q., ZHANG, Y., DUAN, H. & HE, X.T. 2016 Molecular dynamics simulations of microscopic structure of ultra strong shock waves in dense helium. *Front. Phys.* **11**, 1–11.
- LIU, H., ZHANG, Y., KANG, W., ZHANG, P., DUAN, H. & HE, X.T. 2017 Molecular dynamics

- simulation of strong shock waves propagating in dense deuterium, taking into consideration effects of excited electrons. *Phys. Rev. E* **95** (2), 023201.
- LIU, Z., SONG, J., XU, A., ZHANG, Y. & XIE, K. 2023 Discrete Boltzmann modeling of plasma shock wave. *Proc. Inst. Mech. Eng. Part C J. Mech. Eng. Sci.* **237** (11), 2532–2548.
- MOSS, J. N. & BIRD, G. A. 2005 Direct simulation Monte Carlo simulations of hypersonic flows with shock interactions. *AIAA J.* **43** (12), 2565–2573.
- PHAM-VAN-DIEP, G., ERWIN, D. & MUNTZ, E. P. 1989 Nonequilibrium molecular motion in a hypersonic shock wave. *Science* **245** (4918), 624–626.
- QIU, R., BAO, Y., ZHOU, T., CHE, H., CHEN, R. & YOU, Y. 2020 Study of regular reflection shock waves using a mesoscopic kinetic approach: Curvature pattern and effects of viscosity. *Phy. Fluids* **32** (10), 106106.
- QIU, R., YANG, X., BAO, Y., YOU, Y. & JIN, H. 2024 Mesoscopic kinetic approach of nonequilibrium effects for shock waves. *Entropy* **26** (3), 200.
- QIU, R., YOU, Y.C., ZHU, C.X. & CHEN, R.Q. 2017 Lattice Boltzmann simulation for high-speed compressible viscous flows with a boundary layer. *Appl. Math. Model.* **48**, 567–583.
- QIU, R., ZHOU, T., BAO, Y., ZHOU, K., CHE, H. & YOU, Y. 2021 Mesoscopic kinetic approach for studying nonequilibrium hydrodynamic and thermodynamic effects of shock wave, contact discontinuity, and rarefaction wave in the unsteady shock tube. *Phys. Rev. E* **103** (5), 053113.
- RANA, A. S., SAINI, S. AND CHAKRABORTY, S., LOCKERBY, D. A. & SPRITTLES, J. E. 2021 Efficient simulation of non-classical liquid-vapour phase-transition flows: a method of fundamental solutions. *J. Fluid Mech.* **919**, A35.
- REYHANIAN, E., DORSCHNER, B. & KARLIN, I. 2023 Exploring shock-capturing schemes for particles on demand simulation of compressible flows. *Comput. Fluids* **263**, 105947.
- RINDERKNECHT, H. G., AMENDT, P.A. AND WILKS, S.C. & COLLINS, G. 2018 Kinetic physics in ICF: present understanding and future directions. *Plasma Phys. Control. Fusion* **60** (6), 064001.
- SAWANT, S. S., THEOFILIS, V. & LEVIN, D. A. 2022 On the synchronisation of three-dimensional shock layer and laminar separation bubble instabilities in hypersonic flow over a double wedge. *J. Fluid Mech.* **941**, A7.
- SCHWARTZENTRUBER, T. E. & BOYD, I. D. 2015 Progress and future prospects for particle-based simulation of hypersonic flow. *Prog. Aerosp. Sci.* **72**, 66–79.
- SHAKHOV, E. M. 1968 Generalization of the krook kinetic relaxation equation. *Fluid Dyn.* **3** (5), 95–96.
- SHAN, L., WU, F., YUAN, Z., WANG, W., CAI, H., TIAN, C., ZHANG, F., ZHANG, T., DENG, Z., ZHANG, W. & OTHERS 2021 Research progress of kinetic effects in laser inertial confinement fusion. *High Power Laser Part. Beams* **33** (1), 012004.
- SHAN, Y. 2024 Non-equilibrium kinetics effects in shock and detonation: based on the discrete Boltzmann method. *Doctoral dissertation* .
- SHAN, Y., XU, A., WANG, L. & ZHANG, Y. 2023 Nonequilibrium kinetics effects in Richtmyer-Meshkov instability and reshock processes. *Commun. Theor. Phys.* **75** (11), 115601.
- SHI, C., HAN, W., DEITERDING, R., ZHU, C. & YOU, Y. 2020 Second-order curved shock theory. *J. Fluid Mech.* **891**, A21.

- SHOEV, G., KOKHANCHIK, A.A., TIMOKHIN, M. Y. & BONDAR, Y. A. 2017 Stationary regular reflection: Viscous and rarefaction effects. In *30th International Symposium on Shock Waves 1: ISSW30-Volume 1*, pp. 685–689. Springer.
- SOD, G. A. 1978 A survey of several finite difference methods for systems of nonlinear hyperbolic conservation laws. *J. Comput. Phys.* **27** (1), 1–31.
- SONG, J., XU, A., MIAO, L., CHEN, F., LIU, Z., WANG, L., WANG, N. & HOU, X. 2024 Plasma kinetics: Discrete Boltzmann modeling and Richtmyer-Meshkov instability. *Phys. Fluids* **36** (1).
- SONG, J., XU, A., MIAO, L., LIAO, Y., LIANG, F., TIAN, F., NIE, M. & WANG, N. 2023 Study on entropy increase characteristics of shock wave/plate laminar boundary layer interaction. *Acta Aeronaut. Astronaut. Sin.* **44** (21), 528520.
- STRUCHTRUP, H. 2005 *Macroscopic Transport Equations for Rarefied Gas Flows: Approximation Methods in Kinetic Theory*. Springer, Heidelberg.
- STRUCHTRUP, H. & TORRILHON, M. 2003 Regularization of Grad's 13 moment equations: Derivation and linear analysis. *Phys. Fluids* **15** (9), 2668–2680.
- SUCCI, S. 2018 *The lattice Boltzmann equation: for complex states of flowing matter*. Oxford university press.
- TIMOKHIN, M. Y., KUDRYAVTSEV, A.N. & BONDAR, Y. A. 2022 The mott-smith solution to the regular shock reflection problem. *J. Fluid Mech.* **950**, A14.
- WANG, Y. & WANG, Y. 2024 Unsteady interaction and dynamic stability analysis of a two-stage-to-orbit vehicle during transverse stage separation. *Acta Astronaut.* **216**, 488–503.
- WANG, Y., WANG, Y. & JIANG, Z. 2023 Unsteady interaction mechanism of transverse stage separation in hypersonic flow for a two-stage-to-orbit vehicle. *Phys. Fluids* **35** (5).
- WANG, Y., WANG, Y. & JIANG, Z. 2024 Experimental and numerical investigation on the unsteady interaction in longitudinal stage separation for parallel-staged two-body configuration. *Phys. Fluids* **36** (1).
- WANG, Z., WEI, Y. & QIAN, Y. 2020 A simple direct heating thermal immersed boundary-lattice Boltzmann method for its application in incompressible flow. *Comput. Math. Appl.* **80** (6), 1633–1649.
- WANG, Z., WEI, Y. & QIAN, Y. 2022 A novel thermal lattice Boltzmann model with heat source and its application in incompressible flow. *Appl. Math. Comput.* **427**, 127167.
- WEI, Y., LI, Y., WANG, Z., YANG, H., ZHU, Z., QIAN, Y. & LUO, K. H. 2022 Small-scale fluctuation and scaling law of mixing in three-dimensional rotating turbulent Rayleigh-Taylor instability. *Phys. Rev. E* **105** (1), 015103.
- WOODWARD, P. & COLELLA, P. 1984 The numerical simulation of two-dimensional fluid flow with strong shocks. *J. Comput. Phys.* **54** (1), 115–173.
- WU, L., ZHANG, J., REESE, J. M. & ZHANG, Y. 2015 A fast spectral method for the Boltzmann equation for monatomic gas mixtures. *J. Comput. Phys.* **298**, 602–621.
- XU, A., ZHANG, D. & GAN, Y. 2024 Advances in the kinetics of heat and mass transfer in near-continuous complex flows. *Front. Phys.* **19** (4), 42500.
- XU, A., ZHANG, G.C., GAN, Y.B., CHEN, F. & YU, X.J. 2012 Lattice Boltzmann modeling and simulation of compressible flows. *Front. Phys.* **7**, 582–600.
- XU, A. G. & ZHANG, Y. D. 2022 *Complex Media Kinetics*. Science Press.

- XU, K. 2014 *Direct modeling for computational fluid dynamics: construction and application of unified gas-kinetic schemes*, , vol. 4. World Scientific.
- XU, K. & HUANG, J.C. 2010 A unified gas-kinetic scheme for continuum and rarefied flows. *J. Comput. Phys.* **229** (20), 7747–7764.
- YANG, L., SHU, C., WU, J. & WANG, Y. 2016 Numerical simulation of flows from free molecular regime to continuum regime by a DVM with streaming and collision processes. *J. Comput. Phys.* **306**, 291–310.
- YAO, Y., LI, S. G. & WU, Z. N. 2013 Shock reflection in the presence of an upstream expansion wave and a downstream shock wave. *J. Fluid Mech.* **735**, 61.
- ZHANG, D., XU, A., ZHANG, Y., GAN, Y. & LI, Y. 2022 Discrete Boltzmann modeling of high-speed compressible flows with various depths of non-equilibrium. *Phys. Fluids* **34** (8).
- ZHANG, Y., WU, XIAO, NIE, B., XU, A., CHEN, F. & WEI, R. 2023 Lagrangian steady-statlagrangian steady-state discrete Boltzmann model for non-equilibrium flows at micro-nanoscale. *Phys. Fluids* **35** (9).
- ZHANG, Y., XU, A., ZHANG, G., CHEN, Z. & WANG, P. 2019a Discrete Boltzmann method for non-equilibrium flows: Based on Shakhov model. *Comput. Phys. Commun.* **238**, 50–65.
- ZHANG, Y., XU, A., ZHANG, G., GAN, Y., CHEN, Z. & SUCCI, S. 2019b Entropy production in thermal phase separation: a kinetic-theory approach. *Soft Matter* **15** (10), 2245–2259.
- ZHANG, Y., XU, A., ZHANG, G., ZHU, C. & LIN, C. 2016 Kinetic modeling of detonation and effects of negative temperature coefficient. *Combust. Flame* **173**, 483–492.
- ZHAO, W., CHEN, W. & AGARWAL, R. K. 2014 Formulation of a new set of simplified conventional burnett equations for computation of rarefied hypersonic flows. *Prog. Aerosp. Sci.* **38**, 64–75.
- ZHOU, Y. 2017a Rayleigh-Taylor and Richtmyer-Meshkov instability induced flow, turbulence, and mixing. i. *Phys. Rep.* **720-722**, 1–136.
- ZHOU, Y. 2017b Rayleigh-Taylor and Richtmyer-Meshkov instability induced flow, turbulence, and mixing. II. *Phys. Rep.* **723-725**, 1–160.
- ZHU, Y., LIU, C., ZHONG, C. & XU, K. 2019 Unified gas-kinetic wave-particle methods. II. multiscale simulation on unstructured mesh. *Phys. Fluids* **31** (6).